Hindawi
International Journal of Energy Research
Volume 2023, Article ID 5557828, 25 pages
https://doi.org/10.1155/2023/5557828

Research Article

Thermohydraulic and Irreversibility Analyses of Swirl Flows Utilizing Distorted Radial Fins: Entropy Generation and Entransy Dissipation Evaluation

M. L. G. Ho[1], **L.-L. Tan**[2], **Y. M. Hung**[1] **and C. S. Oon**[1]

[1]*Department of Mechanical Engineering, School of Engineering, Monash University Malaysia, Jalan Lagoon Selatan, 47500 Bandar Sunway, Selangor, Malaysia*
[2]*Multidisciplinary Platform of Advanced Engineering, Department of Chemical Engineering, School of Engineering, Monash University Malaysia, Jalan Lagoon Selatan, 47500 Bandar Sunway, Selangor, Malaysia*

Correspondence should be addressed to C. S. Oon; oonsean2280@yahoo.com

Received 10 August 2023; Revised 7 November 2023; Accepted 17 November 2023; Published 21 December 2023

Academic Editor: Mohammadmahdi Abdollahzadehsangroudi

The current investigation analyses the convective heat transfer performance, entropy generation, and entransy evaluation of swirl flows generated by distorted radial fins (DRF). As swirl flows and various vortical structures induce large temperature gradients, second law and entransy analyses are necessary to thoroughly evaluate their true thermodynamic influence on heat transfer enhancement. The results indicated that due to the influence of swirl flows and vortices, all angles of the DRF were capable of inducing intense fluid mixing, thinner thermal boundary layers, and turbulent eddies. It was found that overaggressive swirl flows may hinder local heat transfer performances, by enclosing low-velocity heated fluids within the thermal boundary layers. However, as these overaggressive swirl flows and strong vortices propagate downstream, beneficial fluid mixing was eventuated, favouring heat transport over large regions. In terms of thermal performances, the maximum heat transfer enhancement was exhibited by the $\alpha = 45^{\circ}$ DRF, improving the Nusselt numbers up to 59.3%. Accordingly, the highest performance evaluation criterion (PEC) of 1.269 was obtained by the $\alpha = 45^{\circ}$ DRF at the Reynolds number 2389, attributed to the centrifugal effects of the swirl flows. Optimal entropy generation numbers were also exhibited by the $\alpha = 45^{\circ}$ DRF at the highest studied Reynolds number, reducing total entropy generation by 36.81%. Lower entransy thermal resistances were also accredited to greater DRF angles due to the intense swirl effects. In essence, the study concludes that the effects of swirl flows and vortices significantly enhance heat transfer, whilst reducing both entropy generation and entransy dissipation rates, leading to optimal thermal performances.

1. Introduction

Internal forced convection heat transfer has seen a plethora of applications throughout numerous engineering systems, inclusive of heat exchangers, IC engines, and gas turbine systems [1, 2]. As such, great importance has been placed on enhancing their heat transfer capabilities. There exist two primary techniques for enhancing heat transfer, which are active methods, methods that require input from an external supply of energy, and passive methods, methods that rely on the use of effective heat transfer area, fluid modification, and flow alterations [3]. One of the most common passive methods of heat enhancement is the use of fins or inserts in flow domains. Mainly, the addition of fins or inserts functions to increase the conductive surface area for heating/cooling. However, in recent years, studies have found interesting flow occurrences and heat transfer phenomena due to the presence of fins [4]. These flow structures are simply known as vortices and are classified based on their rotational axis direction [5]. Longitudinal vortices rotate perpendicular to the flow direction, whilst transverse vortices rotate parallel to the flow direction. The creation of such vortical structures has shown immense improvements in heat transfer enhancement, due to various ideal flow characteristics

induced in the flow [6–10]. In spite of the enhanced heat transfer rates, the presence of fins often leads to increased pressure drop and friction losses across the system, which correlates to higher pumping power requirements [11]. Thus, researchers have diverted their attention to creative fin designs that are capable of generating vortical structures whilst sustaining pressure drop. Additionally, the combined effects of modified geometry and nanofluids have shown compelling heat transfer performances [12–14].

The generation of vortices is primarily due to the pressure difference between the freestream flow and the resulting pressure after interaction with a blockage in the flow. Transverse vortices are typically due to flow separation, which is defined as the detachment of the boundary layers from the body surface, where the reattachment eventuates a recirculation zone, brimmed with transverse vortices [15]. The generated recirculation zone is due to the pressure difference, which pulls and impinges the flow inwards, creating transverse vortices. Longitudinal vortices are due to the pressure difference between the upstream and downstream sides of the fin, inducing perpendicular rotational motion, which can eventuate swirling effects to the main flow direction [16]. Several studies have been conducted on longitudinal and transverse vortices individually and have reported compelling results. Zheng et al. investigated the thermohydraulic effects of longitudinal swirl flows utilizing internally grooved tubes and found that the swirl flows eventuated by the longitudinal vortices highly disturbed the flow fields, leading to significant heat transfer enhancement [17]. Oon et al. numerically analysed flow separation utilizing a backward-facing step [18]. They found that the lowest temperature was located near the end of the recirculation zone, signifying maximum local heat transfer within the transverse vortical structures. Wang et al. found similar results when investigating the effects of perforated curve fins within an annular domain [19]. The observed results suggested that lower temperatures emerged within regions of strong and large vortices, regardless of the types of vortices. Jiang et al. examined the heat transfer enhancement of a plate heat exchanger with symmetrically distributed capsules [20]. The results indicated that both transverse and longitudinal vortices promoted swirling that disrupted the boundary layers, effectively enhancing heat transfer rates. The study concluded that vortices and fluid impingement were the primary contributors to heat transfer enhancement. Although the presence of the vortical structures promoted swirling, the influence of swirl flows was lacking within the study, where thorough evaluation of the effects of swirling flows could have been the primary contributor to the thermohydraulic performance. Chompookham et al. attempted to study the heat transfer effects of a wedge-ribbed channel using winglet vortex generators [21]. The authors found significant heat transfer enhancement mainly due to two factors, which are continual interruption of the thermal boundary layer achieved by recirculating flows and longitudinal vortices that channelled the reverse flow trapped behind the ribs into the freestream flow. From the literature, it is commonly known that longitudinal vortices possess superior heat transfer capabilities compared to transverse vortices [7], likely due to the swirling effect often associated with longitudinal vortices. These swirling effects, fittingly known as swirl flows, possess incredible heat transfer capabilities, due to the intense centrifugal fluid mixing over large regions of the fluid domain. Nair et al. [6] investigated the heat transfer performance of swirl-inducing fins. The authors found that due to the swirling longitudinal vortices, higher recirculation intensity was effectuated, leading to increments in local heat transfer coefficient and the Nusselt numbers. However, the authors failed to conclude if swirl flow intensity directly correlates to better heat transfer performances. Furthermore, intense, long-lived swirl flows are difficult to achieve, due to the influence of the constant freestream flow [22]. Thus, in order to produce prominent and prolonged swirling effects, the simultaneous generation and company of vortical structures could potentially strengthen and perpetuate swirl flows, whilst intensifying turbulence. The current paper is aimed at employing fins that are capable of producing intense swirl flow, strengthened by vortices, in order to determine its thermohydraulic influence and assess the correlation between swirl flow intensity and heat transfer performance.

Historically, one of the main assessors of heat transfer performance is the performance evaluation criteria (PEC), which takes into consideration of the frictional losses. It is defined as the ratio between the Nusselt number improvement and friction factor penalties of employed heat transfer enhancement methods and a baseline case without any methods employed. Various studies have utilized this approach for diverse thermal engineering applications as an optimization technique [23–26]. Besides this, complex flows involving large temperature gradients are often investigated utilizing first law analysis for thermodynamic evaluation. However, this approach does not sufficiently address the complexity of effective energy dissipation and transfer mechanisms [27, 28]. This necessitates second law analysis as an approach to investigate such losses and the true thermodynamic influence of the heat transfer enhancement method. The second law of thermodynamics expresses that all real processes are irreversible by nature, where entropy is a measurement of irreversibility and is directly proportional to destroyed exergy [29]. This suggests that as entropy is generated, energy quality deteriorates. Therefore, in order to preserve energy quality, or minimize entropy generation, it is critical to study entropy generation distribution in thermofluid processes. Shiba and Bejan proposed a method to close the gap between thermodynamics, heat transfer performance, and fluid dynamics [30]. Subsequently, entropy generation minimization (EGM) emerged as an approach for optimal thermal system designs. Numerous investigations have been conducted on second law analysis and EGM, to optimize thermal system performances [31–35]. Mwesigye et al. numerically analysed the effects of longitudinal vortices generated by surface-detached twisted tapes [36]. The study found that the twisted tape inserts effectuated a major reduction in entropy generation, especially at low Reynolds numbers, which determined the optimum Reynolds number for each specific case. Similar to most literature, the authors primarily focused on the entropy generation due to geometrical

effects, instead of the entropy generation due to the flow phenomena. The comprehension of entropy generation due to flow phenomena is immensely pertinent, as second law analysis and overall fluid dynamics are fundamental in every thermal system. Korei and Benissaad [37] evaluated the entropy generation of nanofluid flow through a 90° elbow. The study varied the Reynolds number, nanoparticle concentration, and nanoparticle diameter. In all cases, it was found that the addition of nanoparticles led to a reduction of entropy generation, where an increment in the Reynolds number led to a reduction in viscous entropy and an increase in thermal entropy. Similar results were also obtained by Duangthongsuk and Wongwises [38] when analysing the thermal effects of conical strip inserts on EGM. Interestingly, it was found that the maximum studied Reynolds number generated the lowest entropy, obtaining vastly dissimilar results from other studies. Although EGM and second law analysis have also been applied in recent efforts studying modified geometries and nanofluid [39–42], second law investigation on intense and specific fluid phenomena has been lacking within the current state of the art, necessitating the current paper. Furthermore, as intense swirl flows and vortices significantly influence the temperature distribution, energy dissipation, and local flow velocities, second law analysis could provide a deeper comprehension of the overall thermodynamics' improvement of swirl flows and vortical structures on heat transfer and fluid mechanics.

Coupled with second law analysis, Guo et al. [43] proposed the novel concept of entransy, which describes the potential capability of convective heat transfer. This could be elucidated as the amount of energy transferred is conserved and the potential of transferring heat is reduced due to thermal resistances. Thus, for any heat transfer process between two mediums, the higher temperature medium loses entransy, whilst the other lower temperature gains entransy [44]. Hence, as the concept of entransy is not conserved in heat transfer, entransy dissipation expresses the loss of potential heat transfer capability due to irreversibilities and could also be utilized as another assessor to specifically evaluate the efficiency of convective heat transfer. Both entransy and entropy are important, as the concept of entropy is related to irreversibilities during heat-work conversion, whilst entransy is the concept of irreversibilities during convective or conductive heat transfer without work [45]. This signifies that entransy dissipation expresses the quantitative irreversibilities purely due to temperature differences between mediums, by formulating a form of thermal resistance for entransy. Thus, the development of the entransy dissipation extremum principles, which states the primary objective of optimization for heat transfer processes, involves minimizing entransy dissipation rate (EDR) and entransy thermal resistance (ETR). Several studies have implemented entransy evaluation as an approach to optimize heat transfer processes [46–48]. All of which reflects the importance that the minimalizing of ETR indefinitely leads to optimal heat transfer. Broadly, state-of-the-art literature has primarily utilized this approach for optimization of specific thermal systems, where investigations on the entransy dissipation of fluid phenomena, such as swirl flows and vortical structures, are yet to be conducted. Without of which, the fundamental optimization of convective heat transfer cannot be achieved. Thus, the current work is conducted to establish the entransy dissipation rate and thermal resistance of swirl flows and vortices for optimal convective heat transfer.

Although numerous studies have conducted the separate thermohydraulic effects of swirl flows and vortices, investigation on the interactions of long-lived, intense swirl flows that are instantly strengthened by vortices has yet to be thoroughly assessed. Furthermore, the correlation between swirling intensity and thermohydraulic performance remains unexplored. Hence, the current study is aimed at designing fins that are capable of generating profound swirling flows and vortical structures, by implementing various distortions and blockages, fittingly known as distorted radial fins (DRF). The analysis contributes to filling the research gap, by conducting a numerical analysis on heat transfer enhancement due to the combined effects of swirl flows and various vortical structures, to determine their thermohydraulic benefit and evaluate the relationship between swirl flows and heat transfer. Presently, little work has been conducted on irreversibility analysis, such as entropy and entransy, for fluid phenomena, whereas previous works merely implemented first law analysis and have not comprehensively considered the irreversible losses of swirl flows due to entransy dissipation and entropy generation. Thus, second law analysis and entransy evaluation are conducted to assess the true thermodynamics and convective thermal resistances of the studied fin design when generating intense swirl flows and vortical structures. Explicitly, the novelty and work innovation of this work lie in the evaluation of the heat transfer enhancement when combining the effects of swirl flows and vortices, conducting a second law analysis for these effects, and evaluating the ETR of the generated fluid phenomena.

2. Methodology

2.1. Computational Model. Figure 1 depicts an example of the computation models for the current investigation, which is the case of the 15° angle of attack (α) DRF. The entire length of the annular channel is 1.5 m, where the centre length of 1.2 m is subjected to a constant heat flux of 20804.57 W/m^2. The remaining walls such as the outer wall and inner walls near the inlet and outlet possess adiabatic boundary conditions. Five sets of DRF were employed, with seven radial fins per set. Each individual radial fin possesses a thickness of 2 mm, a length of 6 mm, and a height of 4.34 mm, corresponding to 10.72 mm fin diameter. The radial fins were created by initially setting the base of the fins onto the inner pipe, with the face of the fin facing the spanwise direction, and distorting the front face of the fin clockwise at the amplitude. The distortion of the fin extends until the amplitude of the fin faces the streamwise direction, perpendicular to the flow direction. Five angles of attacks are studied, where the base angle of individual radial fins is angled at 0°, 15°, 25°, 35°, and 45°, where the amplitude of the fins is kept unchanged perpendicular to the flow, for all angles of attack. The distance between each set of DRF is

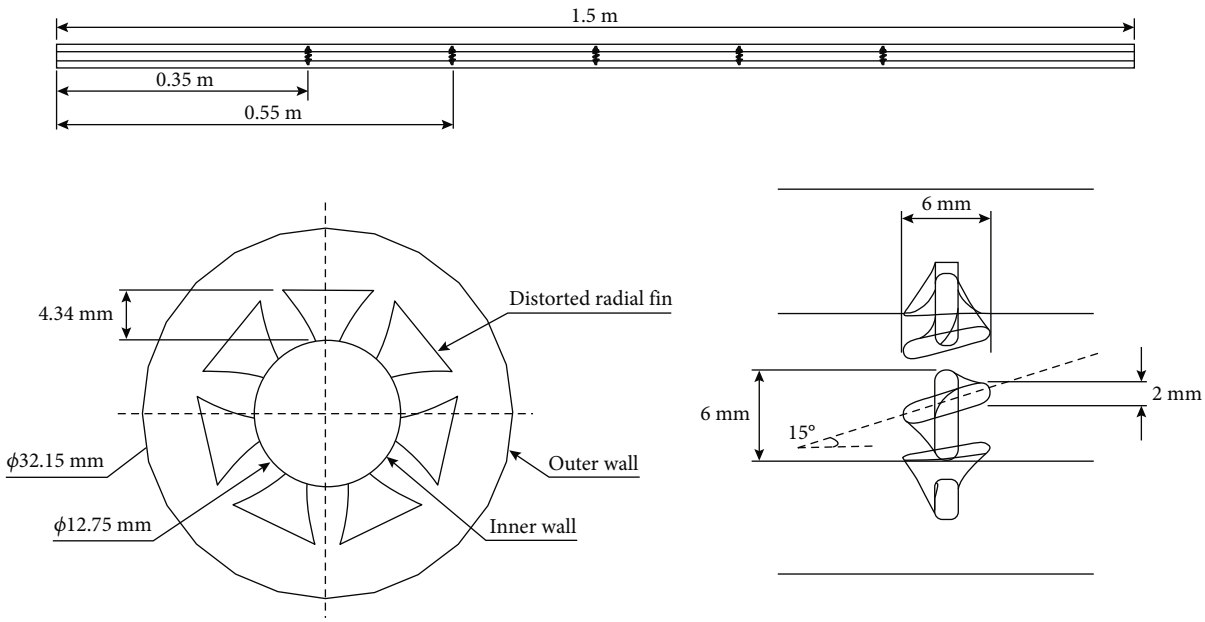

(a) Two-dimensional side and front view of the annular channel consisting of five (5) DRF sets ($\alpha = 15^{\circ}$)

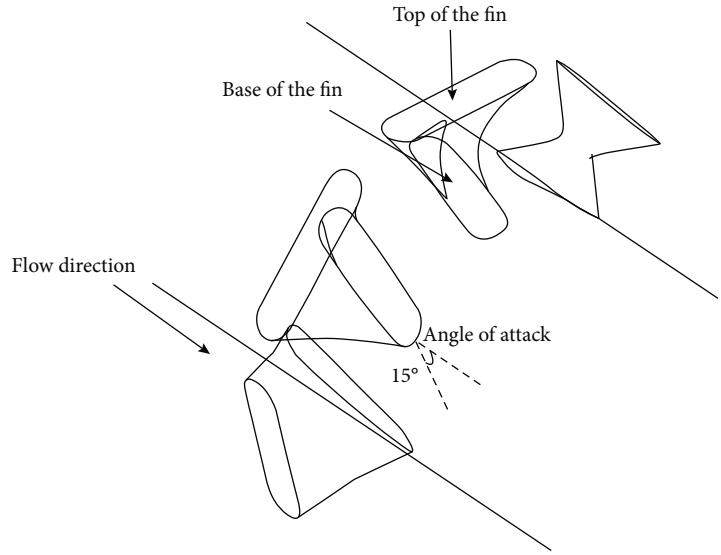

(b) Three-dimensional view and anatomy of the individual DRF ($\alpha = 15^{\circ}$)

Figure 1: Schematics and dimensions of the DRF computation model ($\alpha = 15^{\circ}$).

kept at 0.2 m, where the first set and last set of DRF possess a distance of 0.35 m from the inlet and outlet, respectively. The geometric details of the studied models are provided in Table 1. Due to the presence of the DRF located on the heated inner pipe, conductive boundary conditions on the fins are employed. The boundary conditions utilized for the current investigation are summarized in Table 2. The Reynolds number range considered for the current study lies within the transitional and turbulent regime and ranges from 2389 to 10752, which corresponds to a flow rate range of 4–18 l/min.

2.2. Numerical Simulations. In order to simulate and predict complex turbulent flows, the current investigation is analysed utilizing ANSYS FLUENT 2022 R1. The algorithm solution method utilized to solve the Navier-Stokes equation, which solves for the momentum and energy fluxes within the computational model, was the semi-implicit pressure-linked equation-consistent (SIMPLEC) scheme. Furthermore, a second-order upwind discretization method was also applied for the pressure, momentum, and turbulence equation to achieve more precise and reliable solutions. The viscous sublayer equations were addressed utilizing the shear-stress transport (SST) k-ω turbulence model, selected distinctively due to its robust and accurate projection of the fluid phenomena near the vicinity of the wall. The transport equations governing turbulent kinetic energy, k, and specific dissipation rate, ω, within the SST

Table 1: Geometric details of the investigated fin models.

Geometric details	Value
Total length, L (m)	1.5 m
Heated length, L_H (m)	1.2 m
Outer pipe diameter, D_o (mm)	32.15 mm
Inner pipe diameter, D_i (mm)	12.75 mm
Number of fin sets	5 sets
Number of fins per set	7 radial fins
Fin thickness (mm)	2 mm
Fin height (mm)	4.34 mm
Fin length (mm)	6 mm
Fin angle of attacks, α	0°, 15°, 25°, 35°, and 45°

Table 2: Summary of boundary conditions.

Parameter	Boundary condition
Inlet	Velocity inlet
Outlet	Pressure outlet
Outer wall	Adiabatic
Inner wall (near the inlet and outlet)	Adiabatic
Heated section of inner wall	Constant heat flux (20804.56772 W/m^2)
Distorted radial fins	Conductive
Inlet fluid temperature	293.15 K
Reynolds number	2,389–10,752

k-ω turbulence model, are elucidated in the following equations [49].

$$\frac{\partial(\rho u_i k)}{\partial x_i} = \frac{\partial}{\partial x_j}\left[\Gamma_k \frac{\partial k}{\partial x_j}\right] + G_k - \beta' \rho k\omega, \tag{1}$$

$$\frac{\partial(\rho u_i \omega)}{\partial x_i} = \frac{\partial}{\partial x_j}\left[\Gamma_\omega \frac{\partial \omega}{\partial x_j}\right] + G_k + D_w - \beta \rho \omega^2. \tag{2}$$

The current model is employed due to its credible simulation on separated boundary layers, which are critical in heat transfer investigations. This is primarily because the SST turbulence model is capable of segregating the flow domain into two regions, comprised of the near wall region and the free stream region. The blending function of the model then switches between the k-ω and k-ε models in their respective preferred regions [50]. This function of the turbulence model is vital for heat transfer studies, as it ensures proper capture of the phenomena within the laminar boundary layer, allowing for a more accurate depiction of heat transfer in fluid flow. Furthermore, the model allows for exceptionally accurate results relative to other turbulence models and has proven to exhibit consistent agreement with experimental findings [51, 52]. As for the fluid, distilled water at 293.15 K is utilized for all the numerical simulations, where the properties are procured and summarized in Table 3 [53]. Prior to the employment of the conservation of energy equations, several assumptions were adopted for the numerical simulations.

Table 3: Thermophysical properties of distilled water [53].

Thermophysical property	Value
Density, ρ (kg/m^3)	998.5
Viscosity, μ (kg/m·s)	0.00079
Specific heat capacity, C_p (J/kg·K)	4182
Thermal conductivity, k (W/m·K)	0.6024
Prandtl number, Pr	5.484

(i) A three-dimensional computational domain analysis is conducted

(ii) Incompressible, steady-state flow, with constant thermophysical fluid properties, was employed

(iii) Gravitational effects were assumed at $y = -9.81$ m/s^2

(iv) No-slip conditions are assumed for the walls of the computational domain

These assumptions were adopted to minimize computation expense whilst highly prioritizing accuracy. The absence and presence of gravitational effects were tested for all the Reynolds numbers for the case of the smooth pipe and DRF $\alpha = 0°$. The rationale for the test was to study the influence of buoyancy force, which could slightly affect the numerical results, especially within the laminar regime. Thus, due to the presence of buoyancy force and natural convection, gravitational effect was assumed. The three-dimensional Navier-Stokes equations for incompressible flows, consisting of the conservation of mass, momentum, and energy, are described in Equations (3)–(7) [54]. The governing equations for continuity, momentum, and energy are written in cylindrical coordinates due to the cylindrical nature of the model.

Continuity equation:

$$\frac{1}{r}\frac{\partial(rV_r)}{\partial r} + \frac{1}{r}\frac{\partial V_\theta}{\partial r} + \frac{\partial V_z}{\partial z} = 0. \tag{3}$$

Momentum equation with respect to r:

$$\frac{\partial V_r}{\partial t} + V_r\frac{\partial V_r}{\partial r} + \frac{V_\theta}{r}\frac{\partial V_r}{\partial \theta} + V_z\frac{\partial V_r}{\partial z} - \frac{V_\theta^2}{r} = -\frac{1}{\rho}\frac{\partial p}{\partial r} + \frac{\mu}{\rho}\left[\frac{\partial}{\partial r}\left(\frac{1}{r}\frac{\partial}{\partial r}(rv_r)\right) + \frac{1}{r^2}\frac{\partial^2 V_r}{\partial \theta^2} + \frac{\partial^2 V_r}{\partial z^2} - \frac{2}{r^2}\frac{\partial V_r}{\partial \theta}\right] + S_r. \tag{4}$$

Momentum equation with respect to θ:

$$\frac{\partial V_\theta}{\partial t} + V_r\frac{\partial V_\theta}{\partial r} + \frac{V_\theta}{r}\frac{\partial V_\theta}{\partial \theta} + V_z\frac{\partial V_\theta}{\partial z} + \frac{V_r V_\theta}{r} = -\frac{1}{\rho r}\frac{\partial p}{\partial \theta} + \frac{\mu}{\rho}\left[\frac{\partial}{\partial r}\left(\frac{1}{r}\frac{\partial}{\partial r}(r v_\theta)\right) + \frac{1}{r^2}\frac{\partial^2 V_\theta}{\partial \theta^2} + \frac{\partial^2 V_\theta}{\partial z^2} + \frac{2}{r^2}\frac{\partial V_r}{\partial \theta}\right] + S_{\theta.} \tag{5}$$

Momentum equation with respect to z:

$$\frac{\partial V_z}{\partial t} + V_r\frac{\partial V_z}{\partial r} + \frac{V_\theta}{r}\frac{\partial V_z}{\partial \theta} + V_z\frac{\partial V_z}{\partial z} = -\frac{1}{\rho}\frac{\partial p}{\partial z} + \frac{\mu}{\rho}\left[\frac{1}{r}\frac{\partial}{\partial r}\left(r\frac{\partial V_z}{\partial r}\right) + \frac{1}{r^2}\frac{\partial^2 V_z}{\partial \theta^2} + \frac{\partial^2 V_z}{\partial z^2}\right] + S_z. \tag{6}$$

Energy equation:

$$\frac{\partial i}{\partial t} + \frac{1}{r}\frac{\partial (r V_r i)}{\partial r} + \frac{1}{r}\frac{\partial (V_\theta i)}{\partial r} + \frac{\partial (V_z i)}{\partial z} = -\frac{1}{\rho}\rho\nabla.u + \frac{1}{\rho}\nabla.(\mathrm{k}\nabla\mathrm{T}) + \frac{1}{\rho}\Phi + \frac{1}{\rho}S_i, \tag{7}$$

where the S terms, in this case, are defined as the source terms, describing the initial boundary conditions, and the i term is the internal energy of the fluid. The energy dissipation function, Φ, can be expanded and represented in

$$\Phi = \mu\left\{2\left[\left(\frac{\partial V_r}{\partial r\cos\theta}\right)^2 + \left(\frac{\partial V_\theta}{\partial r\sin\theta}\right)^2 + \left(\frac{\partial V_z}{\partial z}\right)^2\right] + \left(\frac{\partial V_r}{\partial r\sin\theta} + \frac{\partial V_\theta}{\partial r\cos\theta}\right)^2 + \left(\frac{\partial V_r}{\partial z} + \frac{\partial V_z}{\partial r\cos\theta}\right)^2 + \left(\frac{\partial V_\theta}{\partial z} + \frac{\partial V_z}{\partial r\sin\theta}\right)^2\right\} + \lambda(\nabla.u)^2. \tag{8}$$

In order to ensure that a sufficient and reliable grid is chosen for the computational domain, a mesh independence study was performed. The mesh independence study would establish consistent results that are independent of the number of mesh whilst balancing computational resources for the numerical simulations. The current mesh independence study employs the Richardson extrapolation method, with a refinement ratio of 1.3 [55]. The mesh independence study was performed on the DRF at $\alpha = 0^\circ$, at the highest flow rate and Reynolds number, Re = 10,752. The discretized computational model, comprised of tetrahedral meshes with 15 inflation layers set for the walls and fins, is expressed in Figure 2(a) for DRF $\alpha = 0^\circ$ and $\alpha = 45^\circ$. The amount of inflation layers utilized for the current investigation functioned to achieve adequate $y+$ values that would approximately equate to 1 and to sufficiently capture the boundary layers for all simulated flow rates. The inflation layers' growth rates were conserved at 1.2, where the first layer thickness of the walls and fins was set at 0.015 mm and 0.014 mm, respectively. Accordingly, the regions surrounding critical regions, such as the fins and heated wall section, are discretized with finer mesh elements, as a means to maximize coverage on the flow and heat transfer characteristics. Three mesh sizes were analysed, inclusive of the course, medium, and fine mesh sizes, with numbers of elements of 3916348, 8486232, and 18963526, respectively. As depicted in Figure 2(b), the average Nusselt number and pressure drop difference between the course and medium mesh were found to be 12.25% and 4.56%, respectively. However, when refining from the medium to fine mesh, the relative difference in the average Nusselt number and pressure drop reduces to 2.55% and 2.26%, respectively. To maximize computation resources and accurate findings, the medium-sized mesh is deemed sufficient for the current investigation. However, to provide additional evidence of the reliability of the medium-sized mesh, an ultrafine mesh was employed with an increased number of elements of 20501957, in which the average Nusselt number and pressure drop between the ultrafine and fine mesh were 1.54% and 0.44%, respectively. Furthermore, the difference between the medium and ultrafine was merely 4.05% and 2.71%. As the differences between the results were less than 5%, despite having such large discrepancies between the number of elements for the medium and ultrafine mesh, evidence of the computational accuracy of the medium mesh is further substantial. Thus, after extensive consideration to balance computational resource, time, and reliable findings, the medium-sized mesh was selected.

2.3. Data Reduction

2.3.1. Heat Transfer Performance. The following section contributes to process the results obtained from the numerical methodology. In order to evaluate the heat transfer of any system, the convective heat transfer coefficient must first be derived. The heat transfer coefficient can be obtained utilizing the heat flux, inner wall temperature, and bulk temperature of the fluid. Equation (9) represents the average heat transfer coefficient and is simply defined as the quantitative characteristics of convective heat transfer for a given temperature change, whereas Equation (10) describes the equation for bulk temperature and is defined as the energy-average fluid temperature across the fluid domain [56].

$$\bar{h} = \frac{q''}{(T_w - T_b)}, \tag{9}$$

$$T_b = \frac{T_i + T_o}{2}, \tag{10}$$

where q'' represents the heat flux per unit length, whilst T_w, T_b, T_i, and T_o represent the wall, bulk, inlet, and outlet temperature, respectively. Accordingly, the hydraulic diameter of the annular channel and the average Nusselt number can then be computed utilizing Equation (11) and Equation (12), respectively [57]. The hydraulic diameter can be defined as the characteristic diameter of noncircular conduits, typically as a ratio of the cross-sectional area and the

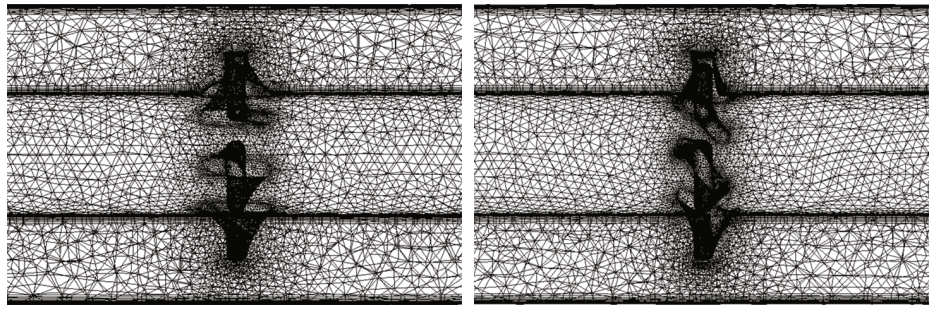

(a) Enlarged view of the discretization of the DRF $\alpha = 0^{\circ}$ (left) and $\alpha = 45^{\circ}$ (right) near the midsection, of the medium mesh size, with roughly 8,486,232 number of elements. The consistency and gradual uniformity of the inflation layers and elements can be observed

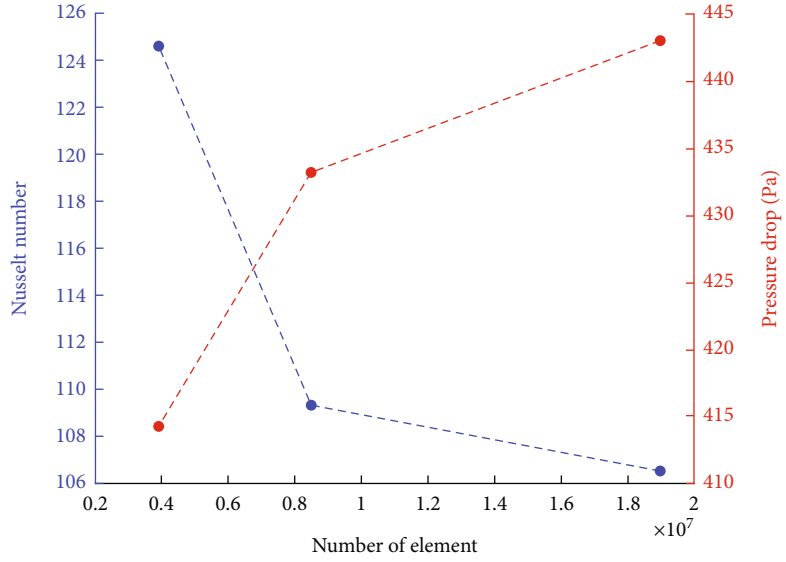

(b) Nusselt number and pressure drop variation against number of elements for $\alpha = 0^{\circ}$ at Re = 10,752

FIGURE 2: Mesh independence study utilizing the Richardson extrapolation method with refinement ratio of 1.3, on the DRF ($\alpha = 0^{\circ}$), at Re = 10,752. The simulated results depict minor discrepancies with increasing number of elements, confirming mesh independence.

wetted perimeter, whereas the Nusselt number is dimensionless and is often defined as the ratio of convective heat transfer to conductive heat transfer.

$$D_h = 2(r_o - r_i), \tag{11}$$

$$\overline{\mathrm{Nu}} = \frac{q_{\mathrm{convective}}}{q_{\mathrm{conductive}}} = \frac{\bar{h} D_h}{k}, \tag{12}$$

where r_o, r_i, and D_h denote the outer pipe radius, inner pipe radius, and hydraulic diameter, respectively. The k term in Equation (12) is the thermal conductivity of the working fluid. Equation (13) elucidates the equation to procure the Reynolds number and is defined as the ratio of inertial forces to viscous forces within a fluid [58].

$$\mathrm{Re} = \frac{\rho U D_h}{\mu}, \tag{13}$$

where ρ represents the density of the fluid, U is the flow velocity, and μ is the dynamic viscosity. Utilizing Darcy Weisbach's pressure drop equation in Equation (14), the friction factor could be obtained. The friction factor is another dimensionless number utilized to define the pressure loss due to the frictional interaction between the fluid flow and the channel walls.

$$f = \frac{2\Delta P D_h}{L \rho v^2}. \tag{14}$$

Finally, the PEC can be calculated utilizing the average Nusselt number and friction factors, defined in Equation (15). The PEC describes the ratio of improved heat transfer ratio and increased friction factor ratio [59]. It factors the heat transfer gain and frictional losses in order to thoroughly analyse the thermohydraulic benefit when employing heat transfer enhancement methods.

$$\mathrm{PEC} = \frac{\mathrm{Nu}/\mathrm{Nu}_s}{(f/f_s)^{1/3}}, \tag{15}$$

where Nu and f represent the average Nusselt number and friction factor for each specific case, whilst Nu_s and f_s represent the average Nusselt number and friction factor for the case of a smooth annular channel.

2.3.2. Second Law Analysis. The second law analysis is performed following methodologies formulated by Bejan [60] and Ratts and Raut [61]. As aforementioned, the thermophysical properties of the working fluid remain constant, regardless of temperature fluctuations. Thus, the calculation of the second law analysis could simply be adopted by applying the first law of thermodynamics on a control volume of length dx, experiencing constant heat flux from the inner wall to the fluid flow, described in the following.

$$d\dot{q} = q''p\,dx = hpdx(T_s - T_b) = \dot{m}C_p dT, \tag{16}$$

where p and C_p represent the wetted perimeter of the channel and the specific heat capacity, respectively. The specific heat capacity is a thermophysical property detailing the amount of heat required to increase the temperature of the material by one degree Kelvin per unit mass [62]. Utilizing Equation (17), the second and fourth terms of the previous equation can be integrated and modified into Equation (18), as terms such as heat flux and specific heat capacity are assumed to remain constant throughout the channel.

$$\frac{dT}{dx} = \frac{q''p}{\dot{m}c}, \tag{17}$$

$$T(x) = T_i + \frac{q''p}{\dot{m}C_p}x, \tag{18}$$

where $\dot{m}$ is the mass flow rate and x is an arbitrary point. The Stanton number is defined as the ratio of the heat transfer coefficient to the thermal capacity of the fluid and can be expressed in Equation (19), where it could also be utilized by substitution into Equation (18), to simplify and formulate Equation (20) [63].

$$\mathrm{St} = \frac{h}{\rho U C_p}, \tag{19}$$

$$T(x) = T_i + \frac{4\mathrm{St}(T_s - T_b)}{D_h}x. \tag{20}$$

Accordingly, the second law analysis could be applied to the same control volume, formulating the entropy production rate, defined in the following.

$$S_{gen} = \dot{m}ds - \frac{q''}{T + (T_s - T_b)}, \tag{21}$$

where ds can be defined as the internal reversible process for incompressible fluids, described by the Gibbs equation in the following.

$$ds = \frac{C_p dT}{T} - \frac{dP}{\rho T}. \tag{22}$$

Updating Equation (21) with the Gibbs equation, Equation (23) can be formulated.

$$\frac{S_{gen}}{dx} = \frac{\dot{m}C_p 4\mathrm{St}}{D_h}\frac{(T_s - T_b)^2}{\left[T_i + (4\mathrm{St}(T_s - T_b)/D_h)x\right]^2} + \frac{\dot{m}}{\rho[T_i + (4\mathrm{St}(T_s - T_b)/D_h)x]}\left(-\frac{dP}{dx}\right), \tag{23}$$

where the pressure gradient at the end of the right term can be expressed in

$$\left(-\frac{dP}{dx}\right) = \frac{f\rho U^2}{2D_h}. \tag{24}$$

The total entropy generation rate can be determined utilizing Equation (25), where the first and second terms are the entropy generation due to thermal irreversibilities and viscous irreversibilities, respectively. Both terms can be expressed separately in Equation (26) and Equation (27).

$$S_{gen,total} = \frac{\left(q''\right)^2 \pi D_h^2 L}{\mathrm{Nu}kT_b^2} + \frac{8\dot{m}^3 fL}{\pi^2\rho^2 T_b D_h^5}, \tag{25}$$

$$S_{gen,th} = \frac{\left(q''\right)^2 \pi D_h^2 L}{\mathrm{Nu}kT_b^2}, \tag{26}$$

$$S_{gen,f} = \frac{8\dot{m}^3 fL}{\pi^2\rho^2 T_b D_h^5}, \tag{27}$$

where L is the length of the fluid domain. Another parameter worth exploring includes the Bejan number (Be), primarily utilized as a ratio of the contribution of thermal irreversibilities over the total entropy generation. Be values between 0 and 1 and describes the dominant entropy generator between the thermal and viscous terms. When the Be ranges closer to 1, thermal irreversibilities dominate, whereas if Be is lesser than 0.5, viscous entropy dominates. Be is defined in the following.

$$\mathrm{Be} = \frac{S_{gen,th}}{S_{gen,total}}. \tag{28}$$

Lastly, the thermodynamic benefit of the heat transfer enhancement method could be determined by employing the entropy generation number, N_s, which is defined as the $S_{gen,total}$ for each specific case as a ratio to the $S_{gen,total}$ for that of a smooth annular channel. At $N_s < 1$, the thermodynamic system permits lesser irreversibilities, with increased heat transfer. The entropy generation number can be expressed in

$$N_s = \frac{S_{gen,total}}{S_{gen,total_s}}. \tag{29}$$

2.3.3. Principle of Entransy Dissipation. The methodologies proposed by Guo et al. [43] and Wu et al. [64] pioneered the current data reduction for the principle of entransy

dissipation. The basic definition of entransy can be expressed in

$$E = \frac{1}{2} Q_{vh} T = \left[\frac{1}{2} (\dot{m} C_v T) T \right], \tag{30}$$

where Q_{vh} and the bracketed term on the right is the internal thermal energy stored in the fluid, V is the volume, and C_v is the molar heat capacity. It should be worth noting that the molar heat capacity is defined similarly to specific heat capacity, which is the amount of heat required to raise one mole of substance by one degree Kelvin or simply the heat capacity of one mole of a substance [65]. Under constant heat flux, the entransy balance equation for a fluid flowing continuously within a pipe can be expressed as [66]

$$\frac{1}{2} \dot{m} C_p T_o^2 = \frac{1}{2} \dot{m} C_p T_i^2 + \dot{m} C_p (T_o - T_i) T_w - \Delta E, \tag{31}$$

where ΔE is the EDR. The left-hand side of Equation (31) depicts the entransy outflow carried by the fluid medium, whilst the right-hand side represents the entransy inflow, across the channel wall and entransy dissipation. Thus, the EDR can be reorganized and defined as

$$\Delta E = \frac{1}{2} \dot{m} C_p (T_o - T_i)(2T_w - T_i - T_o). \tag{32}$$

The equivalent thermal resistance of multidimensional heat transfer or ETR could then be calculated, for the case of specific heat flux.

$$R_h = \frac{2T_w - T_i - T_o}{2\dot{m} C_p (T_o - T_i)} = \frac{\Delta E}{Q_w^2}, \tag{33}$$

where R_h is the ETR and Q_w is the total heat transfer by the constant heat flux, which can be calculated utilizing the definition of specific heat capacity, defined in the following.

$$Q_w = \dot{m} C_p (T_o - T_i). \tag{34}$$

Equation (33) describes the equivalent convective heat transfer thermal resistance or ETR for specific heat fluxes. The equation expresses that for specific heat fluxes, heat transfer is optimized when entransy dissipation is minimized, due to proportional minimization of equivalent thermal resistance. It should be worth noting that for the boundary condition of a given wall temperature, maximizing entransy dissipation with minimized thermal resistances would lead to optimized heat transfer [67]. In both cases, minimization of ETR is the primary objective. Thus, for the current boundary condition of specific heat flux, the smallest EDR and ETR are often associated with optimal heat transfer performances.

2.4. Numerical Validation. The simulated results for a smooth annular channel were validated utilizing existing theoretical correlations. The simulated Nusselt numbers of the smooth annular channel were compared with the theoretical Nusselt number correlation by Gnielinski, defined in Equations (35)–(40), and Petukhov, defined in Equation (41) [68].

$$\mathrm{Nu}_{Gn} = \frac{(f_{ann}/8)\mathrm{RePr}}{k_1 + 12.7(f_{ann}/8)^{0.5}\left(\mathrm{Pr}^{2/3} - 1\right)} \left[1 + \left(\frac{D_h}{L} \right)^{2/3} \right] F_{ann}, \tag{35}$$

$$k_1 = 1.07 + \frac{900}{\mathrm{Re}} - \frac{0.63}{(1 + 10\mathrm{Pr})}, \tag{36}$$

$$f_{ann} = (1.8 \log_{10} \mathrm{Re}^* - 1.5)^{-2}, \tag{37}$$

$$\mathrm{Re}^* = \mathrm{Re} \frac{(1 + a)\mathrm{In}\, a + \left(1 - a^2\right)}{(1 - a)^2 \mathrm{In}\, a}, \tag{38}$$

$$F_{ann} = 0.75 a^{-0.17}, \tag{39}$$

$$a = \frac{D_i}{D_o}, \tag{40}$$

$$\mathrm{Nu}_{Pe} = \frac{(f/8)\mathrm{RePr}}{1.07 + 12.7(f/8)^{0.5}\left(\mathrm{Pr}^{2/3} - 1\right)}. \tag{41}$$

Furthermore, the friction factors of the simulated results were also validated utilizing the Petukhov and Blasius theoretical correlations, found in the following [8].

$$f_{Pe} = \left(0.79\, \mathrm{In}\left(\mathrm{Re}_{D_h}\right) - 1.64\right)^{-2}, \tag{42}$$

$$f_{Bl} = 0.316\, \mathrm{Re}_{D_h}^{-0.25}. \tag{43}$$

The validation and comparison with the theoretical correlations previously mentioned for a smooth channel are illustrated in Figure 3. From the figure, the simulated Nusselt number exhibits a close resemblance to Gnielinski's theoretical Nusselt number, particularly at high Reynolds numbers. This can be attributed to the recent experimental modifications conducted specifically on an annular domain by Gnielinski, which further improves the accuracy of the correlations. However, the simulated results diverge from the theoretical Nusselt number by the Petukhov correlations, with increasing Reynolds number. This discrepancy is likely due to the difference in the types of conduits utilized, as Petukhov's theoretical correlations primarily consider circular conduits, instead of annular conduits. Such variation could induce significant influences on the heat distribution and fluid friction, which subsequently affects the accuracy of the current numerical result and the theoretical correlations. As a result, the average deviations for the average Nusselt number for the Gnielinski and Petukhov theoretical correlations are 8.17% and 7.71%, respectively. Additionally, the simulated friction factors for the smooth annular channel were also compared with theoretical correlations by Petukhov and Blasius. The simulated friction factor exhibits similar trends with the theoretical friction factors by both correlations, approaching near convergence at the highest studied Reynolds number. This is a result as both friction

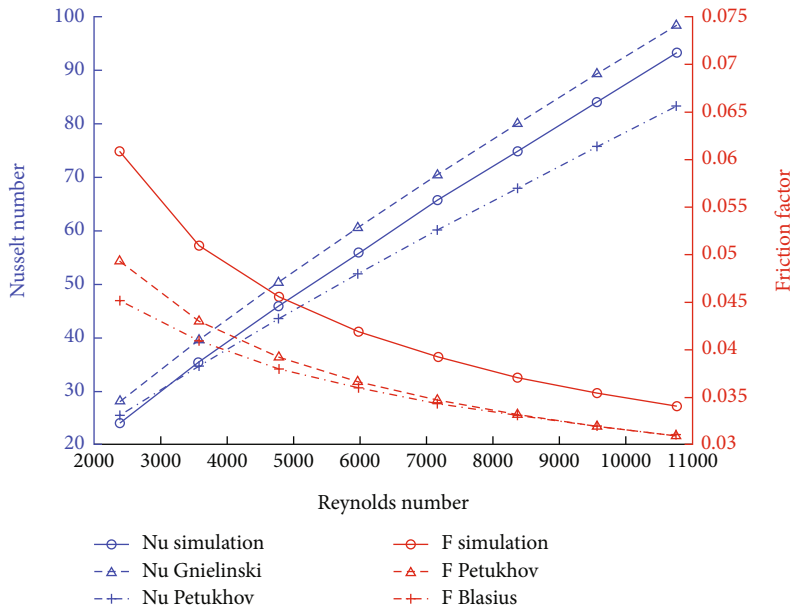

Figure 3: Validation and comparison of the simulated Nusselt number and friction factor with theoretical correlation equations by Gnielinski, Petukhov, and Blasius for a smooth conduit. The simulated results for the Nusselt number and friction factors indicate good agreement with the theoretical correlations.

factor correlations intented use, covers flow regimes above Re = 10,000. The average deviation from the numerical friction factor with the Petukhov and Blasius correlations was 14.88% and 17.76%, respectively. Thus, due to the accurate comparison of the numerical results and theoretical correlations, the computational model is sufficiently accurate and capable of predicting the heat transfer performance utilizing the currently employed computational models.

3. Results and Discussion

3.1. Thermohydraulic Performance Analysis. To compare the thermohydraulic performance of various angled DRF, the average Nusselt number against the Reynolds number is graphically illustrated in Figure 4. Depicted in Figure 4, employing DRF could effectively achieve significant heat transfer enhancement compared to a smooth channel. The thermal enhancement due to DRF is likely due to the generated vortices which intensify turbulence and fluid mixing and further thins boundary layers after each obstacle interaction. Furthermore, due to the curvature and distortion of the DRF, the flow may experience swirling near the heated walls, strengthened by the vortices, which could significantly affect heat transfer augmentation. Accordingly, the swirling effect then increases streamline density and flow velocities near the inner tube and annular regions, resulting in large temperature gradients, continual tearing and thinning of the boundary layers, intense fluid mixing of hot and cold fluids, and, ultimately, heat transfer enhancement. It should be worth noting that the buoyancy force and gravitational effect could also slightly enhance fluid mixing. However, this phenomenon is merely valid for all cases in the laminar regime, while in the transitional and turbulent regime, force convection dominates, leading to negligible gravitational and buoyancy forces. From the figure, higher angled DRF generally exhibits higher heat transfer performances, compared to lower angles. This signifies that heat transport significantly benefits from higher distortion of the DRF, accompanied with more intense fluid phenomena. Interestingly, the $\alpha = 0^\circ$ and $\alpha = 25^\circ$ DRF did not appear to show promising heat transfer results compared to other angled DRF. This may be due to the $\alpha = 0^\circ$ and $\alpha = 25^\circ$ DRF development of unique flow structures that may hinder the generation of swirl flows or vortices that did not contribute to heat transfer enhancement as much as other angles. Another possible phenomenon may be due to the decay of the swirl flows and vortices generated by the $\alpha = 0^\circ$ and $\alpha = 25^\circ$ DRF, which could significantly affect the bulk temperature and pressure gradients, impeding heat transfer. Thus, unique generated flow phenomena and flow regimes, distinctive to each individual angled geometry, could significantly influence heat transfer capabilities. It should be worth noting that at higher Reynolds numbers, the convective heat transfer performance exhibits further enhancement for all cases, due to increased turbulent eddies penetrating the thermal boundary layer, which induces profound fluid mixing. Thus, for incremental Reynolds number, the average Nusselt number exhibits enhancement for all cases. Overall, the employment of the $\alpha = 45^\circ$ DRF achieved the maximum Nusselt number enhancement between 28.9% and 59.3%, compared to a smooth channel.

In terms of hydraulic effects, the influence of DRF on pressure drop and friction factor with various Reynolds numbers is demonstrated in Figures 5(a) and 5(b), respectively. From Figure 5(a), it can be noted that the addition of the DRF significantly alters the pressure drop, especially at higher angles and Reynolds numbers. Accordingly, the friction factor has an inverse relationship with the Reynolds

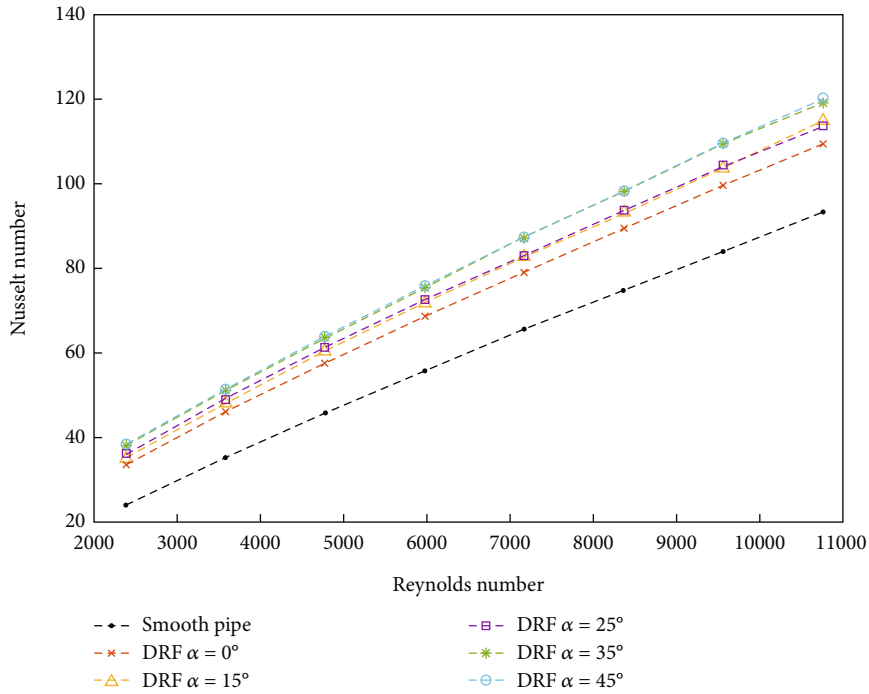

Figure 4: Nusselt number as a function of the Reynolds number for various DRF angles. The figure describes the increasing Nusselt number values with incremental Reynolds numbers.

number, exhibiting diminishing viscous effects with incremental Reynolds number, due to intensified inertial effects that are relative to the viscous effects. From the figures, significant enhancement of pressure drop and friction factors resulted due to the presence of the DRF. For all angles of the DRF, the presence of the fins induces greater fluid resistance to the flow, often accompanied with intensified fluid phenomena that amplified resistances. The vortical structures and swirl flows would then effectuate secondary flows causing additional resistance to the flow. Furthermore, the constant shifting in pressure zones due to the swirling effect, vortical structures, and secondary flows significantly augments momentum, increasing pressure drag forces after each interaction with the DRF, contributing to higher overall pressure loss penalty and friction factors. Amongst the angles of the DRF, the $\alpha = 45^{\circ}$ is shown to possess the highest pressure drop and friction factors. This is due to the relatively larger blockage and distortion of the $\alpha = 45^{\circ}$ fins compared to lower angles, which could possibly lead to fluid stagnation at the leading edges of the fins, resulting in flow hindrance. Thus, the larger blockage yielded more intense swirling effects and higher turbulent intensity, fluid stagnation, and higher pressure gradient, and surface friction viscous dissipation resulted, leading to increased friction factors and pressure drops. Relative to a smooth channel, the maximum friction factor enhancement was 266.8% for the $\alpha = 45^{\circ}$, at Re = 10752.

3.2. Qualitative Thermohydraulic Performance Analysis. In addition to the quantitative analysis of the thermohydraulic performance, a qualitative approach is also conducted to thoroughly visualise the fluid phenomena that contributed to the thermohydraulic performance of various angled DRF. Figure 6 illustrates the temperature contour and the velocity streamlines of the heated walls and fins, for various DRF angles. From the figure, swirl flows are generated after interaction with the DRF, which causes an angular shift of the tangential freestream flow, resulting in a centrifugal effect. The centrifugal effects of the swirl flows then induce turbulent eddies that are capable of continual tearing of the viscous sublayers between the freestream regions and the heated walls, aiding heat transfer between the mediums. The presence of swirl flows enables radial flows, in which the interaction with the tangential freestream flow causes chaotic advection, significantly contributing to intense fluid mixing. As the gaps between each individual DRF tighten associated with increased DRF angles, the tangential freestream flow accelerates, leading to more chaotic and intense swirl flows. Furthermore, due to the streamwise blockage at the amplitude of the fin, transverse vortices are created which forces inward impingement of the freestream flow towards the heated walls. During the impingement process, colder fluids within the freestream flow are integrated with the hot fluids near the heat wall regions, whilst simultaneously, the heated fluids near the inner wall are driven into the freestream region. Thus, due to the generation of the transverse vortices and centrifugal effects of swirl flows, the cold fluids in the freestream region and the hotter fluids near the heated wall regions experience intensive mixing, eventuating high temperature gradients and thinning boundary layers near the walls, leading to improved heat transfer performances.

From the wall temperature contours, the swirling effects are less effective for local heat transfer at greater angles,

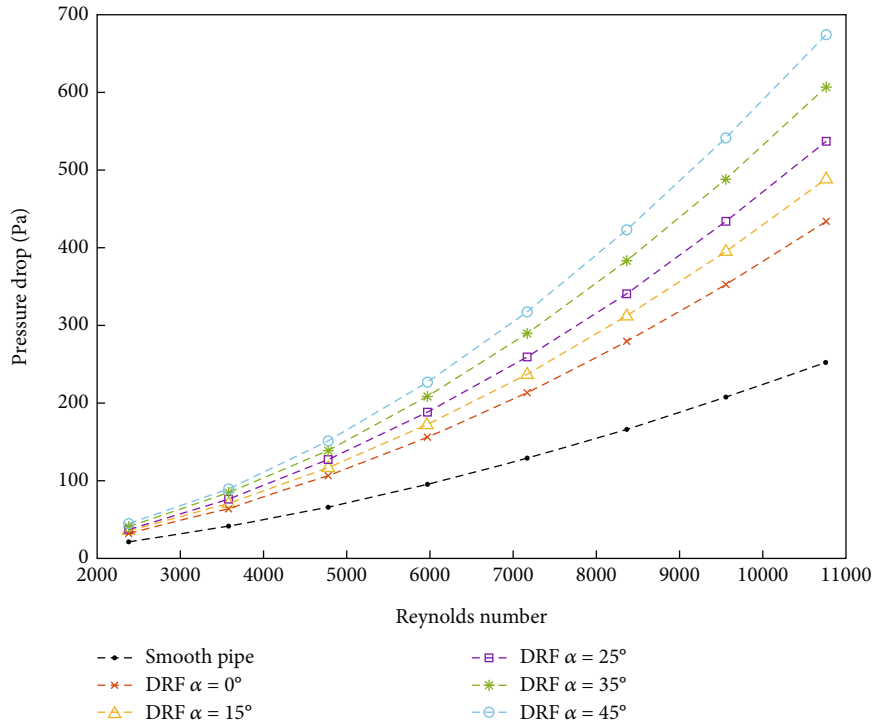

(a) Pressure drop trends across the Reynolds number range. Increments in the Reynolds number and flow velocities exhibit higher pressure drop

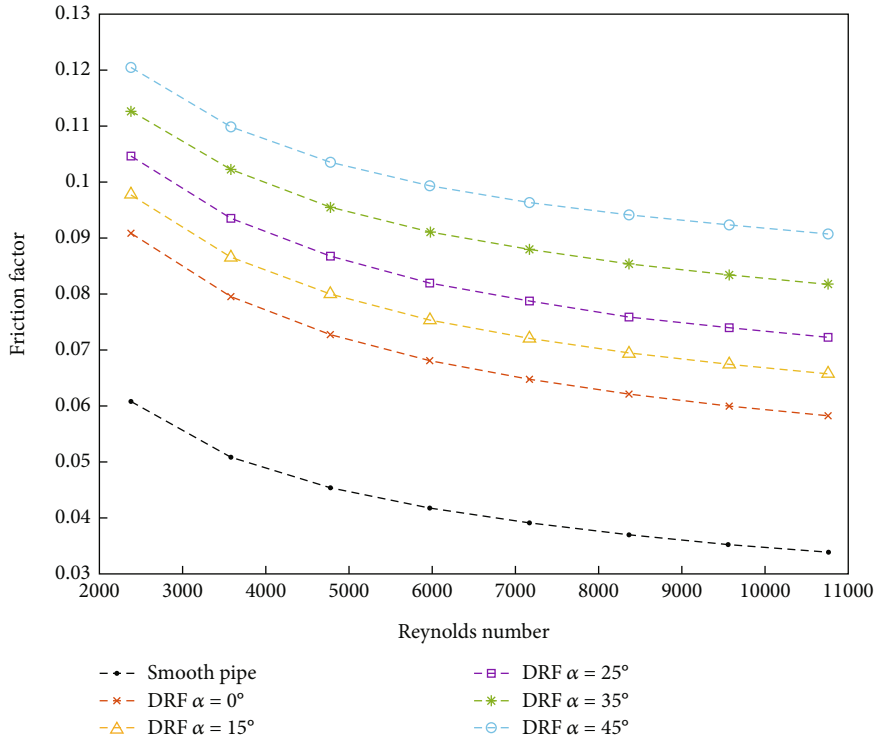

(b) Friction factors of DRF against the Reynolds number. From the figure, an inverse relationship is depicted between the friction factor and Reynolds number

Figure 5: Hydraulic influence of DRF angles, under varying Reynolds number. The figures display higher hydraulic influence with higher angled DRF compared to lower angles.

whereby the $\alpha = 0^{\circ}$ and $\alpha = 15^{\circ}$ have shown more prominent fluid swirl mixing at finned regions. From observation, the figure indicates that higher intensity swirl flows are generated at regions near the trailing edges of high angled DRF fins, whereby the circulation of these intense swirl flows may impinge the flow towards the downwash region, trapping heated fluids within the thermal boundary layer near the fins, which hinder local fluid mixing and heat transfer

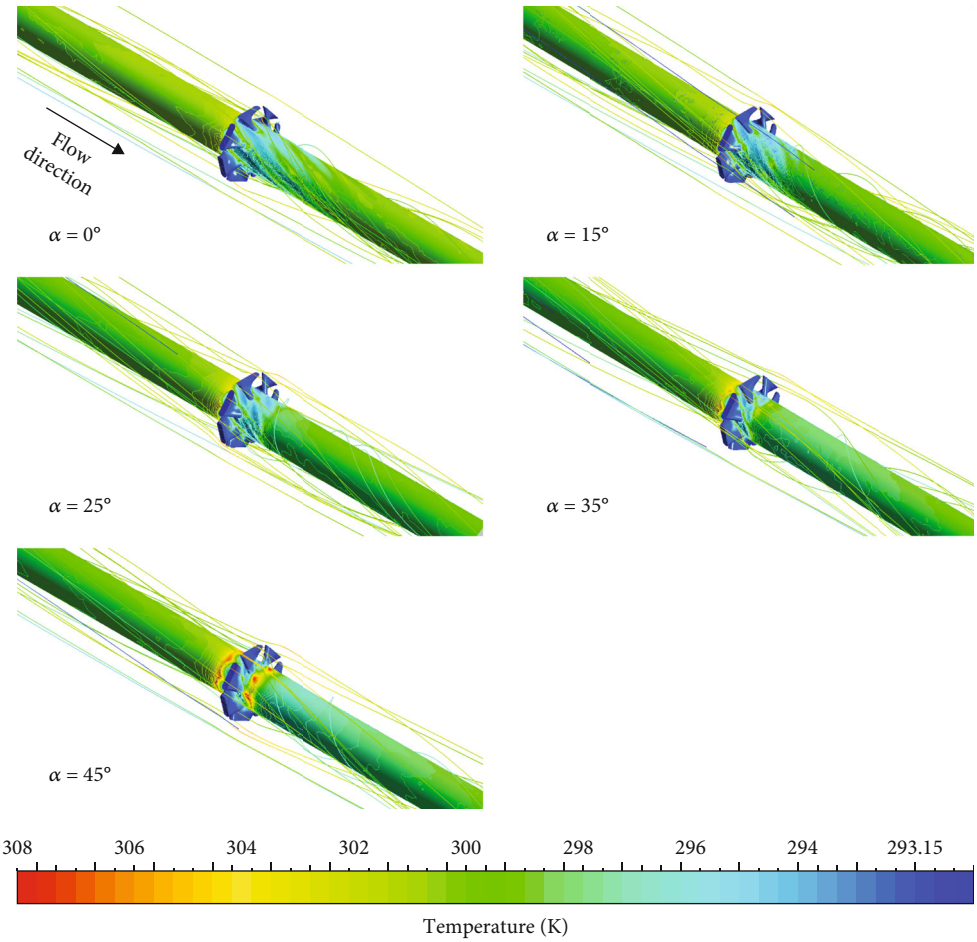

FIGURE 6: Wall temperature contour with velocity flow streamline at Re = 9,558 for various DRF angles (3rd DRF, x between 0.7 m and 0.8 m). Due to the presence of the DRF, prominent swirling effect is effectuated by all angles of the DRF.

performance at the finned regions. It should also be noted that due to the immense blockage and distortion of higher angled DRF, fluid stagnation at the leading edges and backward-flowing vortical structures between the radial fins cause thermal boundary layer thickening, diminishing fluid mixing at the leading edges of the fins, and ultimately resulting in local heat transfer retardation. This is likely because the high blockage of high angled DRF can result in low-pressure regions at the base of leading edges of the fins, which can cause flow hindrance and fluid stagnation. Furthermore, due to the distortion and unique geometry of the DRF, backward-flowing vortices and secondary flows could also develop, coupled with the low-pressure regions; the flow exhibits profound pressure drag, which could impede local heat transfer. These phenomena are illustrated in Figure 6, whereby higher temperatures near the heated walls are exhibited behind and in front of the DRF at higher angles, impeding local heat transfer at leading and trailing edges of the DRF. However, besides the local finned regions, as the swirl flow propagates and eventually decays, significant heat transfer enhancement is exhibited by high angled DRF, over large regions distant from the fins. This is illustrated in Figure 6, in which lower wall temperatures are revealed for higher angled DRF, signifying better heat transfer between the heated wall and fluid medium, due to the aid of intense swirl flows and vortical structures that enabled heat transfer regions beyond the DRF. Overall, despite local heat transfer hindrance at finned regions, swirl flows have shown promising overall heat transfer enhancement, where swirl flow intensity should be highly considered and optimized for individual cases, to achieve optimal heat transfer performances.

Figure 7 depicts the turbulence kinetic energy flooded with flow velocity streamlines. The figure illustrates the effects of the presence of all angled DRF on the turbulent kinetic energy, which is the quantitative measure of turbulence intensity. The presence of the DRF induces high turbulent kinetic energy in regions at the fin tips and midsection of the DRF. This is attributed to the formation of transverse and longitudinal vortices at the fin tips and the swirling effect after each interaction with the fins, which results in increased turbulent kinetic energy in the base and midsection of the annular conduit. Evidence from Figure 7 denotes higher turbulent kinetic energy resulting from higher angled DRF. The mechanism is attributed as higher angled DRF, comprised of tighter flow margins, translates the tangential freestream flow into a centrifugal motion and stronger swirl flows are created, leading to increments in turbulent kinetic

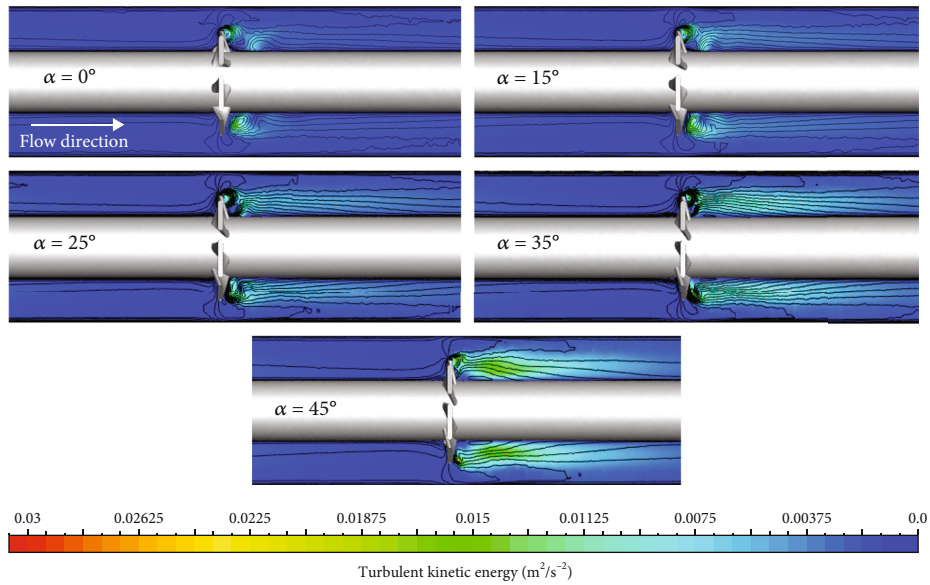

FIGURE 7: Turbulent kinetic energy contour with flow velocity streamlines at Re = 9558 (3rd DRF, x between 0.65 m and 0.8 m). The obstruction and distortion of the DRF forms vortices and eventuates swirl flows, which induces increments in turbulent kinetic energy.

energy. From the observation, stronger vortices were developed by the $\alpha = 25^{\circ}$ and $\alpha = 35^{\circ}$ DRF in comparison with other angles, despite being within the middle range of the studied DRF angles. This implies that distinctive vortical structures are developed with each individual DRF angle, which could uniquely contribute to or hinder swirl flows and heat transfer. This could also rationalise the Nusselt number results of the $\alpha = 0^{\circ}$ and $\alpha = 25^{\circ}$ DRF, in which the vortical structures generated at the leading edges of the fin tips impede the centrifugal effect and overall heat transfer enhancement, especially at higher Reynolds numbers, where vortices could significantly influence swirling and, therefore, thermal performances. Comparing the thermal results with Figure 7 would conclude a direct correlation between higher turbulent kinetic energy due to swirl flows, resulting in higher heat transfer enhancement. However, the significant effects of vortices should not be neglected and could also hinder heat transfer enhancement by impeding the swirl flow or fluid mixing. The results would signify that vortical structures generated by the DRF are primarily located at the fin tips and are inferior, where swirl flow dominates a majority of the freestream region. This would suggest that swirl flows are the primary contributor to heat transfer enhancement, as it dominates fluid mixing at the heated regions, where vortices simply aid and influence the strength of swirl flow.

Figures 8 and 9 depict the Q-criterion with velocity contours of the vortical structures and swirl flows and velocity contour and streamlines in a transverse plane, respectively, at Re = 9558. The Q-criterion, defined as the instantaneous velocity gradient tensor, is utilized to visualise vortical structures. The figure illustrates strong vortical structures being generated at the amplitude of the DRF fins, whilst swirl flows are generated near the midsection of the fin, further confirming the findings in Figure 7. The Q-criterion clarifies that higher angled DRF is capable of generating larger and stronger vortices, followed with more intense swirl flows, compared to lower angles. This further validates that swirl flows are broadly influenced by the flow restriction between each individual DRF, in which turbulent vortical structures may aid or hinder the intensity of swirl flows. Thus, due to the beneficial vortical structures, amplified swirl flows generated by higher angled DRF were capable of higher heat transfer enhancement compared to lower angles. Besides, the figure depicts that the larger and stronger vortices generated by higher angles influencing the centrifugal effect have shown to effectuate low flow velocity regions at the base of the fin. Due to the low flow velocities, stagnant fluids with high temperatures are exhibited near the base of finned regions of high angled DRF. As aforementioned and further depicted in Figures 8 and 9, the strong vortices coupled with intense swirl flows impinge and enclose low-velocity hot fluids within the thermal boundary layer, restricting local fluid mixing, which results in the hindrance of local heat transfer performances. Furthermore, Figure 8 also depicts backward-flowing vortices and secondary flows developing at the base of leading edges of the DRF, which visualises the possibility of heat transfer hindrance due to this phenomenon. Interestingly, as the vortices and swirl flow propagate downstream, the vortices and swirl flows begin to encourage fluid mixing over relatively larger regions, leading to overall enhanced heat transfer. These phenomena are absent for lower angled DRF accredited to weaker swirl flows and vortical structures that quickly dissipate and could not enhance heat transfer, as effective as higher angled DRF. Hence, stronger vortices and swirl flows eventuated by higher angled DRF encourage and yield superior overall heat transfer performances, whilst relatively weaker vortices and swirling effects generated by lower angles that are easily dissipated do not achieve satisfactory overall heat transfer performances. Furthermore, the intense propagated fluid phenomena generated by high angled DRF enables influence

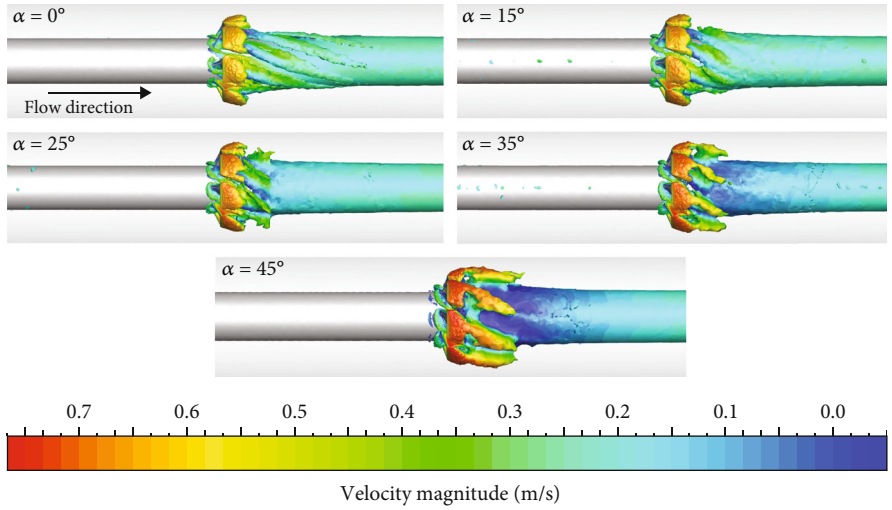

Figure 8: Isosurface Q-criterion with velocity magnitude contour at Re = 9558 (3rd DRF, x between 0.65 m and 0.8 m). The Q-criterion visualises the formation and propagation of vortical structures in turbulent flows. Significant vortical structures and swirling flows are exhibited by all angles of the DRF.

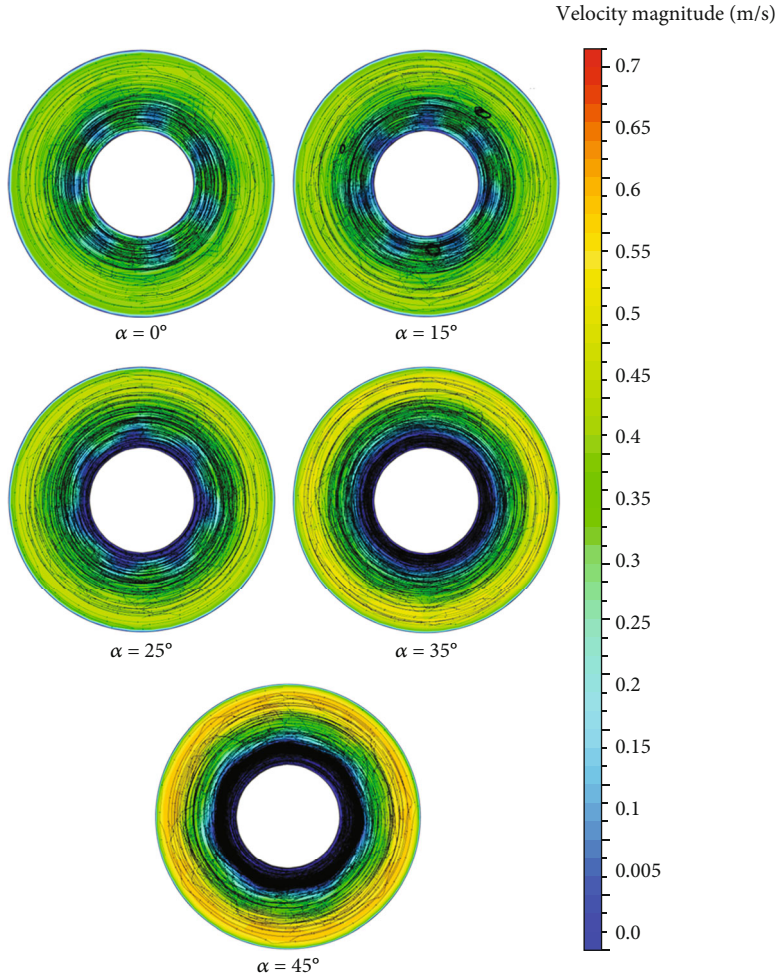

Figure 9: Velocity magnitude contour and streamlines in transverse plane at Re = 9558, downstream of the trailing edge of the 3rd DRF (x = 0.76 m), in which the number of lines in the figure represents the strength of the vortices. Due to the swirl flows, intense vortices eventuate and propagate around the inner wall of the conduit.

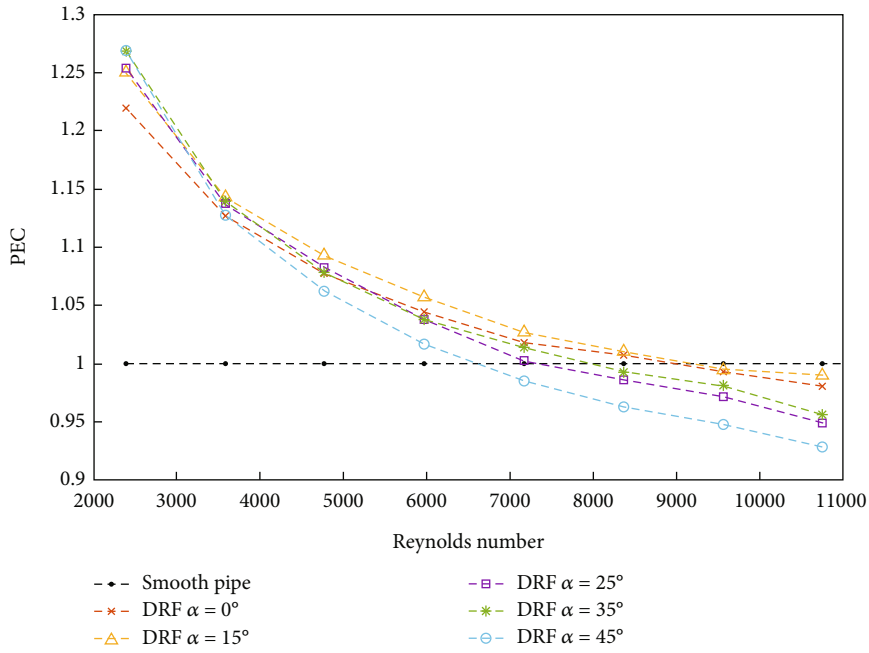

FIGURE 10: Performance evaluation criteria correlation against the Reynolds number range. The straight dotted line at PEC = 1 represents the requirement for equal frictional losses and heat transfer gains of the heat transfer enhancement method, in comparison to the case of a smooth channel or baseline case. The PEC rapidly diminishes with increasing Reynolds number.

on the bulk and wall temperatures far from the DRF, covering and effectuating heat transfer enhancement over large regions of the fluid domain. Dissimilarly, as the relatively weaker swirl flows effectuated by lower angled DRF are generated, the influence of the freestream flow eventually dominates within short distances from the DRF, leading to reduced heat transport at farther regions from the fins. This is depicted in Figures 4 and 6, where the overall quantitative and qualitative thermal transport for high angled DRF is more effective than lower angled DRF. It should be noted that, from Figure 9, minimal vortices are also observed, which may be because vortical structures are very quickly merged into the swirl flows after each interaction with the fins.

3.3. Performance Evaluation Analysis. The PEC assesses specific heat transfer enhancement methods on the heat transfer gains with respect to the fluid friction penalty, compared with that of a smooth channel or baseline case. Figure 10 describes the PEC for various DRF angles against the Reynolds number. From the figure, all DRF angles exhibit deteriorating PEC with incremental Reynolds number. This may be attributed to the exponential enhancement in the intensity of vortices and swirl flows with increasing Reynolds number, which significantly contributes to increased friction factors with diminishing heat transfer gains, resulting in lowered PEC performances. As observed, the highest and lowest PEC was achieved by the $\alpha = 45^{\circ}$ DRF, at the lowest and highest studied Reynolds number, respectively. This signifies that higher angled DRF significantly benefits from low flow rates, creating optimal swirl flow strengths with minimal viscous influence for optimized heat transfer gains. However, compared to lower angles, greater angled DRF also exhibits drastic diminishing results with incremental Reynolds numbers, due to the severe friction factors, owing to relatively larger blockages and overintensified fluid phenomena. At the highest Reynolds number studied, all cases of the DRF exhibit unjustifiable heat transfer gains, obtaining PEC lower than a smooth channel, signifying more frictional losses compared to heat transfer gains of the DRF, relative to the smooth channel. This may be a result of overintensified swirl flows associated with high Reynolds numbers that had depreciating heat transfer enhancement with escalated viscous effects. Another phenomenon worthy of discussion could be the influence of vortices. As vortical structures strongly influence all aspects of the swirl flows, especially at high Reynolds numbers, the formation of turbulent and chaotic vortices could hinder beneficial swirl flows for heat transfer enhancement. This is further exacerbated, as the chaotic vortices also cause increased fluid resistance and drag forces, resulting in further hindrance of the PEC at high Reynolds numbers. Hence, although higher swirling intensity, associated with high Reynolds number and DRF angles, is capable of achieving higher thermal performances, the viscous influence of the phenomenon is often unjustified at high Reynolds numbers. Similarly, at low Reynolds numbers, favourable swirl flows with beneficial vortical structure may have ensued, achieving satisfactory heat transfer gains with minimal fluid friction. In terms of the general trend of the PEC, lower angled DRF have shown slightly better overall results within the studied Reynolds number range. Specifically for the $\alpha = 15^{\circ}$, the angle possessed reasonable heat transfer gains that outweighed fluid friction for a majority of the studied Reynolds number

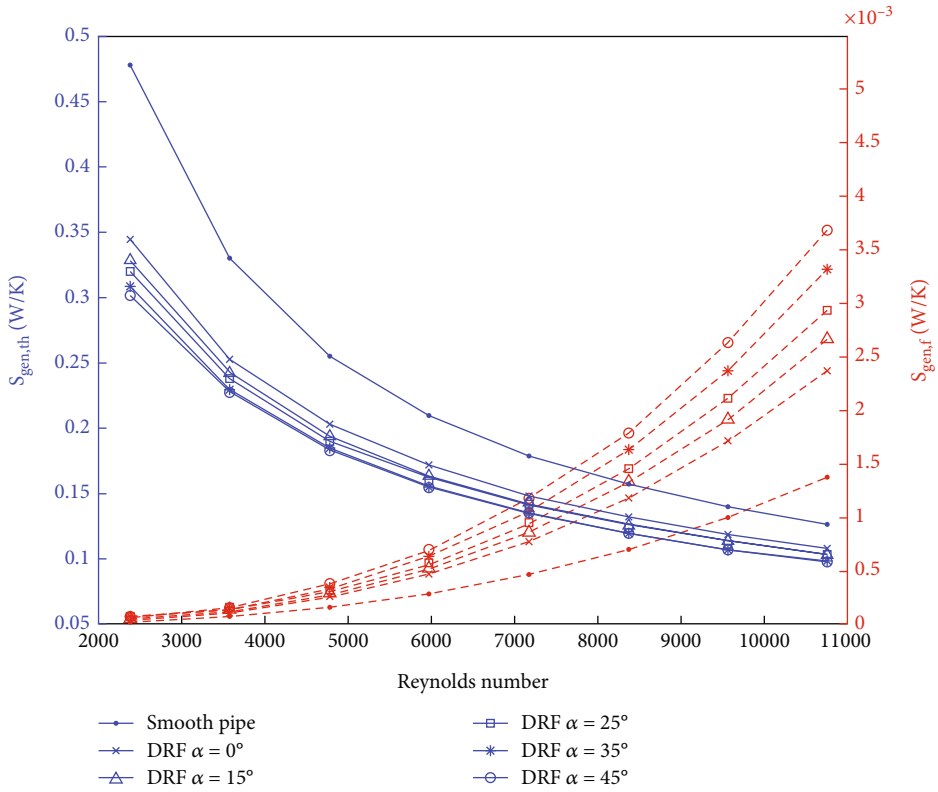

Figure 11: Thermal and viscous entropy generation against various Reynolds numbers. The thermal entropy generation downtrends with increasing Reynolds number, whereas viscous entropy generation intensifies.

range. This may be attributed to the ideal strength and condition of the swirl flow which enabled effective and beneficial fluid mixing, coupled with relatively lesser viscous influence, compared to other angles. Thus, for optimal performance at high Reynolds numbers, lower DRF angles are more advantageous, whereas, in the laminar regime, higher DRF angles are favourable. Despite obtaining the lowest PEC at high Reynolds numbers, the highest PEC of 1.269 was achieved by the $\alpha = 45^{\circ}$, attributed to favourable intensified swirl flow strengths and vortices, with justifiable friction factors, specifically at Re = 2389.

3.4. Second Law Analysis. To comprehend the true thermodynamic nature of the heat transfer enhancement method, second law analysis is required. Second law analysis involves determining entropy generation rate, which occurs due to the presence of irreversibilities. As employment of the DRF may induce large temperature gradients, which could significantly reduce irreversible losses, conducting second law analysis could be utilized as an assessor for optimization and practicality. Figure 11 exemplifies the entropy generation rate due to thermal and viscous irreversibilities with varying Reynolds numbers, for all DRF angles. In terms of thermal entropy generation rate, incremental Reynolds numbers are observed to yield diminishing thermal entropy generation rates for all conduit designs. This is because turbulence and the fluid phenomena intensify with higher Reynolds numbers and amplified fluid mixing and turbulent eddies effectuate, leading to enhanced heat transfer rates. Furthermore, as thermal irreversibilities are inversely proportional to heat transfer rates, higher heat transfer rates and bulk temperatures of the fluid would directly correspond to lower thermal irreversibilities generated. From the figure, the use of DRF has shown significant improvement in thermal EGM, compared to a smooth channel. As observed, lower thermal entropy generation rate can be achieved by employing higher angled DRF. This is attributed to the creation of ideal and intense heat transfer phenomena, such as the centrifugal effects of the swirl flows and vortical structures that reinforced it, which led to overall enhanced heat transfer performance. Indicated previously, as the employment of lower angled DRF yields overall weaker fluid phenomena, marginal heat transfer gains were achieved, resulting in inflated thermal irreversibilities. Thus, the resulting amplified Nusselt number and bulk temperature as a result of higher intensity swirl flows and larger temperature gradients, often incidental to increasing DRF angles, lead to a significant reduction in thermal irreversibilities. In terms of thermal EGM, the best performing case was the $\alpha = 45^{\circ}$, where thermal irreversibilities were reduced by 22.34%–36.81% compared to a smooth conduit. The resulting thermal irreversibilities depict good correspondence to the heat transfer performances from the first law analysis, signifying that lower entropy generation indefinitely leads and corresponds to optimal heat transfer augmentations. Similarly, the figure also depicts the effects of increasing DRF angles and Reynolds number on the viscous entropy generation rates. Evidence suggests that the introduction of

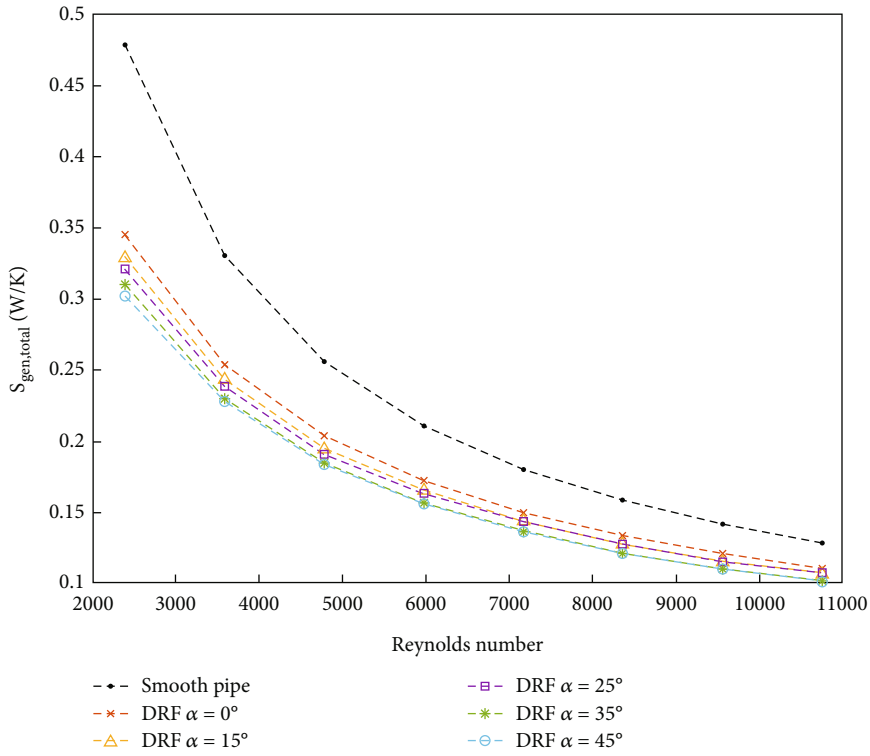

FIGURE 12: Total entropy generation variation with the Reynolds number. From the figure, the dominance of the thermal entropy generation, as the primary contributor to total entropy generation, can be illustrated. Accordingly, the total entropy generation trends similarly to the thermal entropy generation.

greater angled DRF indefinitely results in higher viscous irreversibility generation, in comparison to lower angles. This can be accredited to the immense blockage and fluid occurrences of higher angled DRF, which results in chaotic pressure distribution and increments in the friction factors, significantly affecting the viscous entropy generation rate as stated in Equation (27). Furthermore, as increased flow velocities effectuate rise in the mass flow rates and Reynolds numbers, viscous irreversibilities are enhanced with incremental Reynolds numbers. Hence, due to the direct correlation between blockage, intense fluid occurrences, and viscous irreversibilities, the greatest DRF angle of $\alpha = 45^{\circ}$ exhibited maximum viscous entropy generation rate enhancement up to 266.8% at the highest studied Reynolds number. Figure 12 represents the total entropy generation rate for all conduits, under various Reynolds numbers. The figure clearly illustrates that the total entropy generation rates show similar characteristics with the thermal entropy generation rates, preliminarily implying that total entropy generation is predominantly generated due to thermal irreversibilities, compared to viscous irreversibilities. In essence, the variation of the DRF angles could significantly affect the resulting fluid phenomena, temperature gradients, and pressure distribution, leading to consequential impacts on the Nusselt number, bulk temperature, and friction factors, in which minuscule changes of these circumstances could notably affect the entropy generation rates. Thus, the lowest total entropy generation rates achieved were 0.1021, for the case of $\alpha = 45^{\circ}$ at Re = 10752, accredited to its remarkable heat transfer capabilities.

The Be quantifies the contribution of entropy generation attributed specifically to heat transfer irreversibilities, as a ratio of thermal entropy generation to total entropy generation. Figure 13 describes the distribution of the Be with respect to varying Reynolds numbers and DRF angles. From the results, the Be tends to rapid reduction with incremental Reynolds number, with greater reductions for higher angled DRF. This may result as increasing Reynolds numbers and flow velocities cause significantly greater velocity gradients compared to temperature gradients, which indicates the greater role that viscous irreversibilities play at higher Reynolds numbers. This phenomenon was especially accurate for greater angles, where greater blockages, intense fluid phenomena, and fluid frictions corresponded to greater viscous irreversibilities. The lowest Be of 0.964 was obtained by the $\alpha = 45^{\circ}$ DRF, indicating that, despite operating at the highest studied Reynolds number, thermal entropy dominates and contributes to 96.4% of total entropy generation. Interestingly, at the lowest Reynolds number studied, the highest Be was obtained, at roughly Be = 0.99, which was exhibited by all DRF cases. This can be attributed to two factors: lower viscous irreversibilities generated at low Reynolds numbers and maximum thermal irreversibilities generated at low Reynolds numbers. Hence, at low Reynolds numbers, thermal entropy generation significantly influences entropy generation, whilst the presence of viscous irreversibilities can be

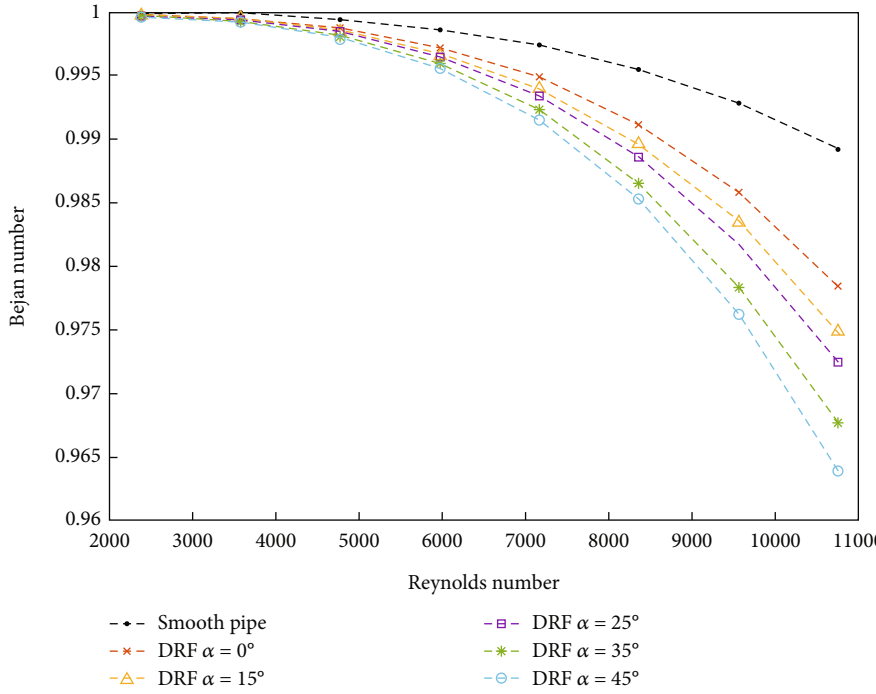

FIGURE 13: Bejan number variation with Reynolds number. The Bejan number analyses the major entropy generation contributor with respect to the total entropy generation, and depicts reduction with incremental Reynolds numbers.

neglected, as it merely contributes to less than 1% of the total entropy generation rate.

Similar to the PEC, the dimensionless entropy generation number could provide insightful information on the thermodynamic benefit of the DRF compared to a smooth channel. As expressed in Equation (29), the primary goal of the entropy generation number is to minimize its value to values at least lower than 1, as it would signify lesser irreversibilities permitted and higher heat transfer gains. As shown in Figure 14, the entropy generation number is plotted against increasing Reynolds numbers. The figure depicts increasing entropy generation number with incremental Reynolds numbers, indicating deteriorating thermodynamic performances with higher flow rates for all DRF angles, compared to that of a smooth channel. The figure also depicts that lower angle suffers from relatively higher entropy generation numbers compared to higher angled DRF. This is a result of higher angled DRF, such as the $\alpha = 45^{\circ}$, generating lower thermal irreversibilities, and as thermal entropy generation dominates the total entropy generation, higher angled DRF results in lower entropy generation numbers compared to lower angles. Thus, despite of higher hydraulic disadvantages, the entropy number generated for higher angled DRF is significantly lower than that of lower angled DRF due to greater intensity of swirl flows which significantly enhanced heat transfer with diminishing thermal entropy generation rates, whereby the optimal entropy number of $N_s = 0.632$ was achieved by the $\alpha = 45^{\circ}$ DRF at Re = 2389, implying that the optimal operating Reynolds number is at Re = 2389 and the employment of the $\alpha = 45^{\circ}$ DRF is capable of reducing total entropy generation up to 36.8%, in comparison to a smooth channel.

3.5. Entransy Evaluation. In order to evaluate the genuine heat transfer performances, purely by convective heat transfer, entransy evaluation must be conducted. Entransy evaluation establishes the thermal potential energy and irreversibilities of heat transfer, at which higher entransy conserved correlates to lower EDR and ETR and, therefore, higher heat transfer performance. Thus, incorporation of entransy evaluation is critical to minimize losses for heat transfer systems, providing quantified statistics on the practicality of various fluid phenomena for heat transfer enhancement. Reduction of entransy due to entransy dissipation and thermal resistances can be obtained utilizing Equation (32) and Equation (33), respectively, which expresses EDR and ETR for turbulent convective heat transfer. Figure 15 shows the effect of incremental Reynolds number with EDR for various DRF angles. From previous sections, the first law analysis determined that heat transfer is enhanced with increasing Reynolds number and DRF angles. Accordingly, with increased heat transfer rates, the thermal potential energy and EDR of the turbulent flows generated by various angled DRF are significantly reduced with incremental Reynolds numbers. This is because the thermal potential energy mainly focuses on the entransy of the wall and, thus, is largely dependent on wall temperatures. Hence, due to the effective convective heat transfer capabilities of swirl flows generated by the DRF, especially at higher Reynolds numbers, the wall temperatures experience massive reduction, resulting in reduced EDR as the heated walls lose temperature. The findings confirm with the theory of entransy, in which the walls lose thermal potential energy with reduction in temperature, whereas the fluid gains thermal potential energy with increased temperatures. This

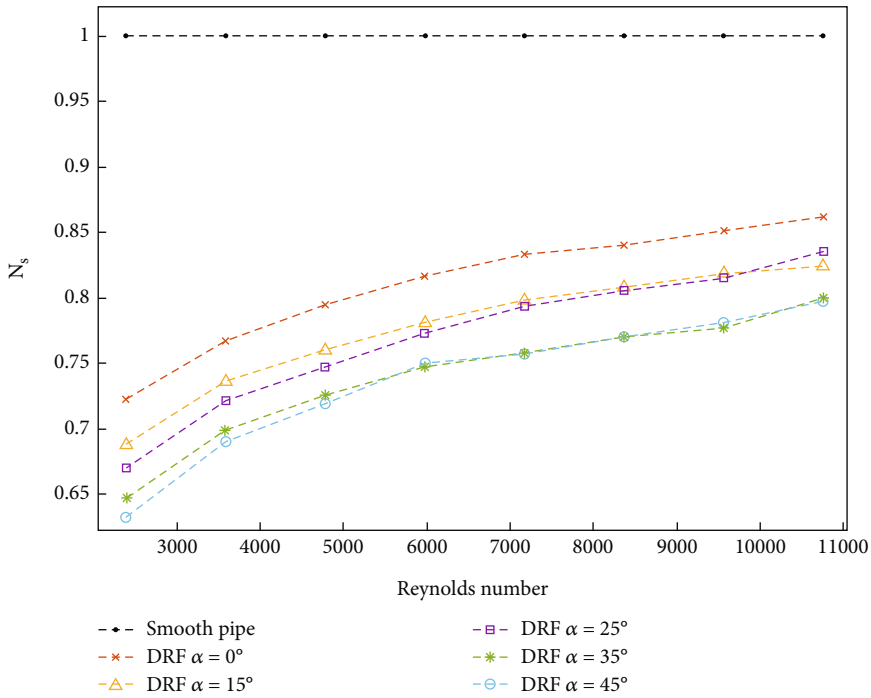

Figure 14: Entropy generation number variation with the Reynolds number. The straight dotted line at $N_s = 1$ represents the minimum value for lesser entropy generation and optimal heat transfer. The figure illustrates direct correlations between the entropy generation number and Reynolds number, especially at higher Reynolds numbers.

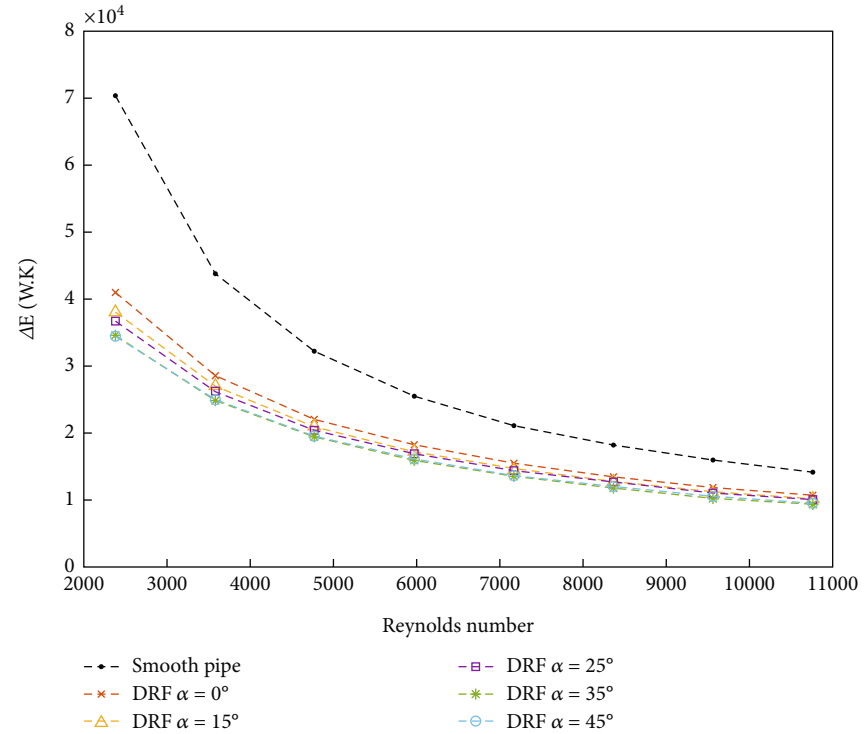

Figure 15: EDR of DRF, under varying Reynolds number. The EDR exhibits depreciation with increasing Reynolds number.

phenomenon is especially evident for higher DRF angles and Reynolds numbers. Interestingly, EDR reduction is noticeably lower and gradually tends to flat at higher Reynolds numbers compared to that at lower Reynolds numbers, for all studied cases. This may be because at low Reynolds number, the flow exhibits weaker turbulence intensity followed

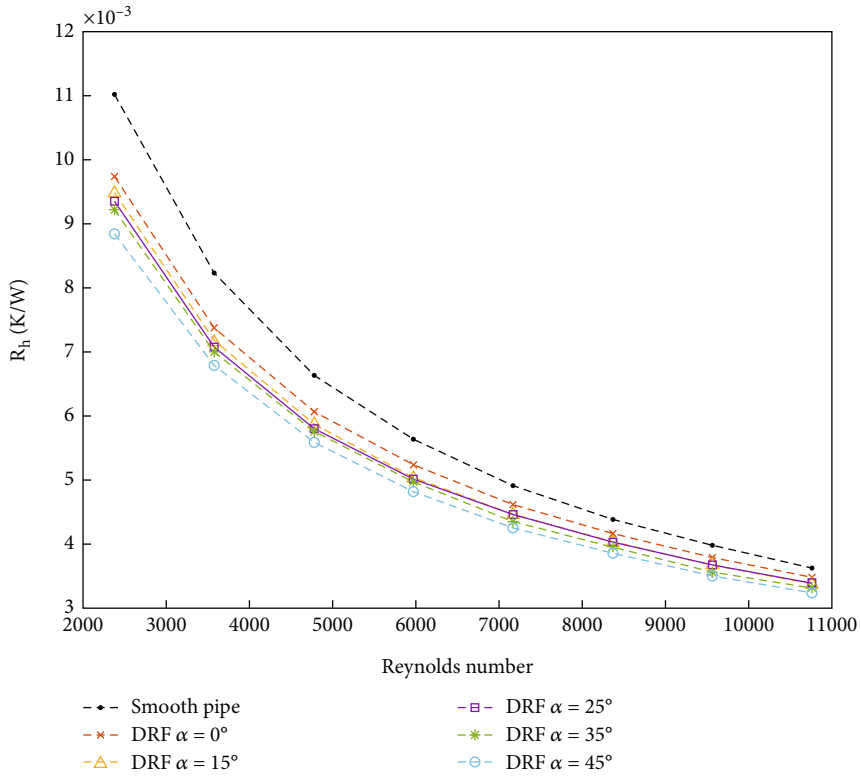

Figure 16: ETR variation with the Reynolds number for different DRF angles. The figure describes a decline in ETR with increments in the Reynolds number.

by relatively weaker swirl flows. Thus, at low Reynolds numbers, convective heat transfer and wall heat dissipation are minimal, resulting in higher EDR. As the EDR tends to flat with incremental flow rates, this may signify the existence of an optimal flow rate, in which a minimum EDR can be achieved, specific for individual cases. Furthermore, the trend also proves that irreversibilities due to entransy dissipation cannot be dismissed, as long as there exists a temperature difference between mediums. This phenomenon is known as the principle of entransy dissipation extremum, whereby the primary goal is to determine the minimum Reynolds number, in which entransy dissipation is at minimum. From the figure, it can be observed that the entransy dissipation extremum occurs near the Reynolds number above 10000, where all DRF angles meet at a point of singularity and the trend tends to flatline, signifying the minimum EDR with maximum heat transfer capabilities.

Figure 16 depicts similar results, with an inverse relationship between ETR and the Reynolds number. Accredited to increased heat transfer capabilities with higher Reynolds numbers, lower ETR is exhibited between the heated wall and the fluid medium. As the lowest ETR corresponds to the best performing DRF angle in terms of heat transfer, Figure 16 indicates that lower ETR favoured higher angled DRF, with the best performing angle being $\alpha = 45^{\circ}$. Similar findings were also established from first law and second law analysis, where Figures 4 and 12 demonstrate that $\alpha = 45^{\circ}$ was the best performing design in terms of average Nusselt number and lowest total entropy generation rate, within the studied Reynolds number range. This denotes that, although local heat transfer is hindered at leading and trailing edges of high angled DRF, due to intense and enduring swirl flows that propagate downstream from the fins, lowering of wall temperatures over larger regions was effectuated, downstream of high angled DRF. Compared to ineffective and weaker swirl flows generated by lower angled DRF, the swirl flows quickly dissipated and decayed over a short distance away from the fins, due to the influence of the free-stream flow, resulting in wall temperature rise after a distance from the fins. This could be observed in Figure 6, whereby cooler and hotter wall temperatures are exhibited by the $\alpha = 45^{\circ}$ and $\alpha = 0^{\circ}$ DRF, respectively, in regions distant from the fins. Furthermore, the increase in wall temperature for the case of the lower angled DRF significantly affected the outlet temperatures and overall EDR, which rationalises the superiority of higher angled DRF, in terms of minimization of ETR. In essence, the lowest EDR and ETR of 9573.25 W·K and 0.00326 K/W, respectively, were achieved by the $\alpha = 45^{\circ}$, at the highest studied Reynolds number, reflecting the lowest generation of convective heat transfer irreversibilities amongst all studied cases. Moreover, the employment of DRF could significantly reduce ETR, up to 19.71%, relative to a smooth channel.

4. Conclusion

The current investigation comprises of an analysis of swirl flows in the heat transfer performances, entropy generation,

and entransy evaluation for radial fins within an annular domain, under various Reynolds numbers. In this paper, the heat delivery performances were mainly attributed to intense swirl flows and vortical structures that significantly influenced the strength and direction of the centrifugal effects. The combined effects of the swirl flows and vortices led to immense improvements in fluid mixing, continual tearing and thinning of boundary layers, and turbulence intensification. The major findings are as follows:

(i) In terms of heat transfer, the $\alpha = 45^{\circ}$ yields superior overall heat transfer performances within the entire Reynolds number range studied, enhancing the Nusselt number between 28.9% and 59.3%

(ii) Intense swirl flows generated by the DRF were capable of impeding local heat transfer by trapping low-velocity and heated fluids within the thermal boundary layer. However, as these intense swirl flows begin to propagate, significant heat transfer enhancement was exhibited over large regions of the fluid domain, compared to relatively weaker swirl flows easily influenced by the freestream flow

(iii) Distinct vortices developed with each individual DRF angle could significantly influence the strength and direction of the swirl flows, impeding or enhancing the centrifugal effect and overall heat transfer enhancement. This suggests that, in the current context, swirl flows are the primary contributor to heat transfer enhancement, where vortices are inferior and merely aid swirling

(iv) The highest PEC of 1.269 was achieved by the $\alpha = 45^{\circ}$ DRF at Re = 2389, due to its effective generated fluid phenomena coupled with reasonable viscous influences

(v) Although the highest entropy generation rates were exhibited at lower Reynolds numbers, in comparison with a smooth pipe, optimal entropy generation number of $N_s = 0.632$ was found at Re = 2389, for the case of the $\alpha = 45^{\circ}$ DRF, signifying a 36.8% reduction in total entropy generation compared to a smooth channel

(vi) Due to the intense swirling effect that encouraged fluid mixing over larger regions, minimum ETR of $R_h = 0.000326$ K/W was achieved by the $\alpha = 45^{\circ}$ DRF at Re = 10752. Thus, the employment of DRF could reduce ETR remarkably, decreasing ETR by up to 19.71%

(vii) In spite of the significant hydraulic effects, the analysis and evaluation from second law and entransy principles found that the $\alpha = 45^{\circ}$ DRF was the optimal DRF angle. The intense swirl flows and vortices enabled significant influence on the bulk, wall, and outlet temperatures, generating lower irreversibilities compared to weaker swirl flows generated by lower angled DRF

(viii) From all three (3) heat transfer optimization analyses, the $\alpha = 45^{\circ}$ DRF was the optimal design, achieving the highest heat transfer enhancement and lowest irreversibility generation rates, attributed to the generation of intense swirl flows, in which the optimal operating Reynolds number was found at Re = 2389 for the first and second law analyses and Re = 10752 for entransy analysis

5. Future Work

The previous discussion has established the significance of various DRF angles, Reynolds numbers, swirl flows, and vortices on the first law, second law, and entransy evaluation. However, with the increasing need for higher heat transfer capabilities, further improvements in future works could substantially push the scientific boundaries of the current study.

(i) From the analysis, further optimization of the geometry of the DRF could be employed. As the DRF, especially at high angles, experiences fluid stagnation at the base of the leading edge due to low-pressure zones, implementing more aerodynamic or streamlined geometries could immensely improve the hydraulic influence of the design

(ii) More thorough analysis on the effects of the DRF parameters could be conducted. Parameters such as the fin height, number of fins per DRF set, fin length, fin thickness, and number of DRF sets in the fluid domain could lead to significant impacts on the fluid phenomena, changing the dynamics of the thermohydraulic performance

(iii) As the DRF has shown to have massive improvements at lower Reynolds numbers, employment of the DRF in natural convection or within low flow rates in the laminar regime could provide more insight into the investigation of swirl flows generated by the DRF. These could unlock untapped knowledge on the effectiveness of swirl flows and the centrifugal effect

(iv) Other forms of application could be explored with the utilization of the DRF and swirl flows, such as microchannel, nuclear applications, or solar applications

(v) The turbulent kinetic energy and turbulence dissipation of swirl flows and vortices could potentially bridge the knowledge gaps in the study of swirl flows and the decay of swirl flows on heat transfer enhancement

(vi) Combined employment of swirl flows and nanofluids could potentially lead to immense heat transfer augmentation, in which the swirl flows could significantly enhance and complement the heat transfer mechanics of nanofluids. This could also bridge the gaps in the impacts and behaviour of swirl flows for non-Newtonian fluids

Nomenclature

Symbols

Be: Bejan number
C_p: Specific heat capacity ($J\,kg^{-1}\,K^{-1}$)
D_i: Inner diameter (mm)
D_o: Outer diameter (mm)
D_h: Hydraulic diameter (mm)
E: Entransy (W.K)
f: Friction factor
h: Heat transfer coefficient (W/m^2K)
k: Thermal conductivity (W/mK)
L: Length (m)
L_H: Heated length (m)
$\dot{m}$: Mass flow rate (kg/s)
Nu: Nusselt number
N_s: Entropy generation number
p: Perimeter (m)
P: Pressure (Pa)
Pr: Prandtl number
q'': Heat flux (W/m^2)
Q: Volumetric flow rate (l/min)
Q_{vh}: Internal energy stored (J)
Q_w: Total heat transfer (W)
R_h: Entransy thermal resistance (K/W)
Re: Reynolds number
$S_{gen,th}$: Thermal entropy generation (W/K)
$S_{gen,total}$: Total entropy generation (W/K)
$S_{gen,f}$: Viscous entropy generation (W/K)
St: Stanton number
T_b: Bulk temperature (K)
T_i: Inlet temperature (K)
T_o: Outlet temperature (K)
T_w: Wall temperature (K)
U: Velocity (m/s).

Greek Symbols

α: Angle of attack (°)
μ: Dynamic viscosity (Pa·S)
ρ: Density (kg/m^3).

Abbreviations

DRF: Distorted radial fins
EDR: Entransy dissipation rate
EGM: Entropy generation minimization
ETR: Entransy thermal resistance
PEC: Performance evaluation criteria.

Data Availability

The extracted data from the numerical simulation can be requested from the first and/or the corresponding author upon request.

Conflicts of Interest

The authors declare that they have no known competing financial interest or personal relationships that could have appeared to influence the work reported in this paper.

Acknowledgments

The authors acknowledge the contribution of the research grant (FRGS/1/2020/TK0/MUM/03/7) provided by the Ministry of Education, Malaysia. Open access publishing is facilitated by Monash University, as part of the Wiley - Monash University agreement via the Council of Australian University Librarians.

References

[1] S. Eiamsa-ard and P. Promvonge, "Thermal characterization of turbulent tube flows over diamond-shaped elements in tandem," *International Journal of Thermal Sciences*, vol. 49, no. 6, pp. 1051–1062, 2010.

[2] M. Bayareh, A. H. Pordanjani, A. A. Nadooshan, and K. S. Dehkordi, "Numerical study of the effects of stator boundary conditions and blade geometry on the efficiency of a scraped surface heat exchanger," *Applied Thermal Engineering*, vol. 113, pp. 1426–1436, 2017.

[3] M. L. G. Ho, C. S. Oon, L. L. Tan, Y. Wang, and Y. M. Hung, "A review on nanofluids coupled with extended surfaces for heat transfer enhancement," *Results in Engineering*, vol. 17, article 100957, 2023.

[4] S. Eiamsa-ard, K. Ruengpayungsak, C. Thianpong, M. Pimsarn, and V. Chuwattanakul, "Parametric study on thermal enhancement and flow characteristics in a heat exchanger tube installed with protruded baffle bundles," *International Journal of Thermal Sciences*, vol. 145, article 106016, 2019.

[5] M. Khoshvaght-Aliabadi, S. Zangouei, and F. Hormozi, "Performance of a plate-fin heat exchanger with vortex-generator channels: 3D-CFD simulation and experimental validation," *International Journal of Thermal Sciences*, vol. 88, pp. 180–192, 2015.

[6] S. R. Nair, C. S. Oon, M. K. Tan, S. Mahalingam, A. Manap, and S. N. Kazi, "Investigation of heat transfer performance within annular geometries with swirl-inducing fins using clove-treated graphene nanoplatelet colloidal suspension," *Journal of Thermal Analysis and Calorimetry*, vol. 147, no. 24, pp. 14873–14890, 2022.

[7] M. Fiebig, "Embedded vortices in internal flow: heat transfer and pressure loss enhancement," *International Journal of Heat and Fluid Flow*, vol. 16, no. 5, pp. 376–388, 1995.

[8] G. Liang, M. D. Islam, N. Kharoua, and R. Simmons, "Numerical study of heat transfer and flow behavior in a circular tube fitted with varying arrays of winglet vortex generators," *International Journal of Thermal Sciences*, vol. 134, pp. 54–65, 2018.

[9] N. Zheng, F. Yan, K. Zhang, T. Zhou, and Z. Sun, "A review on single-phase convective heat transfer enhancement based on multi- longitudinal vortices in heat exchanger tubes," *Applied Thermal Engineering*, vol. 164, article 114475, 2020.

[10] Y. L. He and Y. Zhang, *Advances and Outlooks of Heat Transfer Enhancement by Longitudinal Vortex Generators*, vol. 44, Elsevier, 2012.

[11] K. S. Syed, M. Ishaq, and M. Bakhsh, "Laminar convection in the annulus of a double-pipe with triangular fins," *Computers and Fluids*, vol. 44, no. 1, pp. 43–55, 2011.

[12] M. Sepyani, A. Shateri, and M. Bayareh, "Investigating the mixed convection heat transfer of a nanofluid in a square chamber with a rotating blade," *Journal of Thermal Analysis and Calorimetry*, vol. 135, no. 1, pp. 609–623, 2019.

[13] Z. Korei, S. Benissaad, A. J. Chamkha, F. Berrahil, and A. Filali, "Thermohydraulic and second law analyses during the cooling of an electronic device mounted in an open cavity equipped with magnetic nanofluid, magnetic field inducer, and porous media: a two-phase numerical investigation," *International Communications in Heat and Mass Transfer*, vol. 139, article 106497, 2022.

[14] Z. Korei and N. Bengherbia, "Heat transfer and thermodynamic analysis of the impact of porous media and nanopowder types in an open cavity equipped with an electronic component," *Heat Transfer*, vol. 51, no. 8, pp. 7056–7080, 2022.

[15] C. S. Oon, H. Togun, S. N. Kazi, A. Badarudin, M. N. M. Zubir, and E. Sadeghinezhad, "Numerical simulation of heat transfer to separation air flow in an annular pipe," *International Communications in Heat and Mass Transfer*, vol. 39, no. 8, pp. 1176–1180, 2012.

[16] K. W. Song, S. Liu, and L. B. Wang, "Interaction of counter rotating longitudinal vortices and the effect on fluid flow and heat transfer," *International Journal of Heat and Mass Transfer*, vol. 93, pp. 349–360, 2016.

[17] N. Zheng, P. Liu, F. Shan, Z. Liu, and W. Liu, "Heat transfer enhancement in a novel internally grooved tube by generating longitudinal swirl flows with multi-vortexes," *Applied Thermal Engineering*, vol. 95, pp. 421–432, 2016.

[18] C. S. Oon, H. Togun, S. N. Kazi, A. Badarudin, and E. Sadeghinezhad, "Computational simulation of heat transfer to separation fluid flow in an annular passage," *International Communications in Heat and Mass Transfer*, vol. 46, pp. 92–96, 2013.

[19] Y. Wang, C. S. Oon, J. J. Foo, M. V. Tran, S. R. Nair, and F. W. Low, "Numerical investigation of thermo-hydraulic performance utilizing clove- treated graphene nanoplatelets nanofluid in an annular passage with perforated curve fins," *Results in Engineering*, vol. 17, article 100848, 2023.

[20] C. Jiang, B. Bai, H. Wang, J. Shi, X. Tang, and W. Zhou, "Heat transfer enhancement of plate heat exchangers with symmetrically distributed capsules to generate counter-rotating vortices," *International Journal of Heat and Mass Transfer*, vol. 151, article 119455, 2020.

[21] T. Chompookham, C. Thianpong, S. Kwankaomeng, and P. Promvonge, "Heat transfer augmentation in a wedge-ribbed channel using winglet vortex generators," *International Communications in Heat and Mass Transfer*, vol. 37, no. 2, pp. 163–169, 2010.

[22] Q. Zhang, L. B. Wang, and Y. H. Zhang, "The mechanism of heat transfer enhancement using longitudinal vortex generators in a laminar channel flow with uniform wall temperature," *International Journal of Thermal Sciences*, vol. 117, pp. 26–43, 2017.

[23] H. Moghadasi, E. Aminian, H. Saffari, M. Mahjoorghani, and A. Emamifar, "Numerical analysis on laminar forced convection improvement of hybrid nanofluid within a U-bend pipe in porous media," *International Journal of Mechanical Sciences*, vol. 179, article 105659, 2020.

[24] V. Zimparov, "Energy conservation through heat transfer enhancement techniques," *International Journal of Energy Research*, vol. 26, no. 7, pp. 675–696, 2002.

[25] Y. Khetib, A. Alahmadi, A. Alzaed, M. Sharifpur, G. Cheraghian, and C. Siakachoma, "Simulation of a parabolic trough solar collector containing hybrid nanofluid and equipped with compound turbulator to evaluate exergy efficacy and thermal-hydraulic performance," *Energy Science & Engineering*, vol. 10, no. 11, pp. 4304–4317, 2022.

[26] Y. Wei, S. Zhao, P. Yu, F. Yuan, C. Li, and W. He, "Case studies in thermal engineering comparative studies of fluid mixing and heat transfer behaviors in a millimeter scale T-type mixer with triangular baffles," *Case Studies in Thermal Engineering*, vol. 47, article 103076, 2023.

[27] S. L. Sun, D. Liu, Y. Z. Wang, Y. L. Qi, and H. B. Kim, "Convective heat transfer and entropy generation evaluation in the Taylor- Couette flow under the magnetic field," *International Journal of Mechanical Sciences*, vol. 252, article 108373, 2023.

[28] J. Chen, R. Zhao, Y. Le Nian, and W. L. Cheng, "Numerical study on the effects of cylindrical roughness on heat transfer performance and entropy generation of supercritical carbon dioxide in vertical tubes," *International Journal of Heat and Mass Transfer*, vol. 208, article 124060, 2023.

[29] M. Nemati and A. J. Chamkha, "Examination of effective strategies on changing the amount of heat transfer and entropy during non-Newtonian magneto-nanofluid mixed convection inside a semi-ellipsoidal cavity," *Journal of Magnetism and Magnetic Materials*, vol. 578, article 170652, 2023.

[30] T. Shiba and A. Bejan, "Thermodynamic optimization of geometric structure in the counterflow heat exchanger for an environmental control system," *Energy*, vol. 26, no. 5, pp. 493–512, 2001.

[31] J. V. C. Vargas and A. Bejan, "Thermodynamic optimization of finned crossflow heat exchangers for aircraft environmental control systems," *International Journal of Heat and Fluid Flow*, vol. 22, no. 6, pp. 657–665, 2001.

[32] L. S. Sundar, B. Mathew, A. Sefelnasr, M. Sherif, and A. C. M. Sousa, "Second law of thermodynamic analysis of 40:60% propylene glycol and water mixture based nanodiamond nanofluid under transition flow," *Diamond and Related Materials*, vol. 117, article 108480, 2021.

[33] X. Yang and L. Yang, "Numerical study of entropy generation in fully developed turbulent circular tube flow using an elliptic blending turbulence model," *Entropy*, vol. 24, no. 2, 2022.

[34] S. Morsli, A. Sabeur, and M. El Ganaoui, "Numerical simulation of entropy generation in hydrogen-air burner," *FDMP-Fluid Dynamics & Materials Processing*, vol. 11, no. 4, pp. 342–353, 2015.

[35] M. Bayareh, "Exergy analysis of solar chimney power plants: a review," *Sustainable Energy Technologies and Assessments*, vol. 53, article 102568, 2022.

[36] A. Mwesigye, T. Bello-Ochende, and J. P. Meyer, "Heat transfer and entropy generation in a parabolic trough receiver with wall-detached twisted tape inserts," *International Journal of Thermal Sciences*, vol. 99, pp. 238–257, 2016.

[37] Z. Korei and S. Benissaad, "Turbulent forced convection and entropy analysis of a nanofluid through a 3D 90° elbow using a two-phase approach," *Heat Transfer*, vol. 50, no. 8, pp. 8173–8203, 2021.

[38] W. Duangthongsuk and S. Wongwises, "Comparison of the heat transfer performance and friction characteristics between

fixed and rotating turbine-type swirl generators fitted in a small circular tube," *Experimental Thermal and Fluid Science*, vol. 50, pp. 222–228, 2013.

[39] L. Syam Sundar, "Heat transfer, friction factor and exergy efficiency analysis of nanodiamond-Fe3O4/water hybrid nanofluids in a tube with twisted tape inserts," *Ain Shams Engineering Journal*, vol. 14, no. 9, article 102068, 2022.

[40] M. Bahiraei, N. Mazaheri, M. R. Daneshyar, and A. Mwesigye, "Two-phase simulation of irreversibilities for Ag-water nanofluid flow inside an elliptical pin-fin heat sink: Entropy generation and exergy considerations," *Powder Technology*, vol. 409, article 117723, 2022.

[41] T. Dagdevir and V. Ozceyhan, "A comprehensive second law analysis for a heat exchanger tube equipped with the rod inserted straight and twisted tape and using water/CuO nanofluid," *International Journal of Thermal Sciences*, vol. 181, article 107765, 2022.

[42] Z. Korei, S. Benissaad, A. Filali, and F. Berrahil, "An investigation of entropy and exergy of nanofluid flow in microchannel heat sinks," *Journal of Nanofluids*, vol. 12, no. 4, pp. 1160–1172, 2023.

[43] Z. Y. Guo, H. Y. Zhu, and X. G. Liang, "Entransy-a physical quantity describing heat transfer ability," *International Journal of Heat and Mass Transfer*, vol. 50, no. 13–14, pp. 2545–2556, 2007.

[44] Y. L. He and W. Q. Tao, "Numerical studies on the inherent interrelationship between field synergy principle and entransy dissipation extreme principle for enhancing convective heat transfer," *International Journal of Heat and Mass Transfer*, vol. 74, pp. 196–205, 2014.

[45] X. Chen, T. Zhao, M. Q. Zhang, and Q. Chen, "Entropy and entransy in convective heat transfer optimization: a review and perspective," *International Journal of Heat and Mass Transfer*, vol. 137, pp. 1191–1220, 2019.

[46] Q. Chen, J. Ren, and Z. Guo, "Field synergy analysis and optimization of decontamination ventilation designs," *International Journal of Heat and Mass Transfer*, vol. 51, no. 3–4, pp. 873–881, 2008.

[47] Q. Chen, K. Yang, M. Wang, N. Pan, and Z. Y. Guo, "A new approach to analysis and optimization of evaporative cooling system I: theory," *Energy*, vol. 35, no. 6, pp. 2448–2454, 2010.

[48] Q. Chen, M. Wang, N. Pan, and Z. Y. Guo, "Optimization principles for convective heat transfer," *Energy*, vol. 34, no. 9, pp. 1199–1206, 2009.

[49] W. Luo, H. Han, R. Jiang, R. Yu, and Q. Zhu, "3D numerical investigation of trans-critical heat transfer enhancement in regeneration cooling channel with crescent rib," *International Journal of Thermal Sciences*, vol. 172, article 107287, 2022.

[50] F. R. Menter, "Influence of freestream values on k-omega turbulence model predictions," *AIAA Journal*, vol. 30, no. 6, pp. 1657–1659, 1992.

[51] D. G. Jehad, G. A. Hashim, A. K. Zarzoor, and C. S. N. Azwadi, "Numerical study of turbulent flow over backward-facing step with different turbulence models," *Journal of Advanced Research Design*, vol. 4, no. 1, pp. 20–27, 2015.

[52] A. Boulemtafes-Boukadoum and A. Benzaoui, "CFD based analysis of heat transfer enhancement in solar air heater provided with transverse rectangular ribs," *Energy Procedia*, vol. 50, pp. 761–772, 2014.

[53] L. Syam Sundar, M. K. Singh, and A. C. M. Sousa, "Investigation of thermal conductivity and viscosity of Fe3O4 nanofluid for heat transfer applications," *International Communications in Heat and Mass Transfer*, vol. 44, pp. 7–14, 2013.

[54] H. K. Versteeg and W. Malalasekera, *An Introduction to Computational Fluid Dynamics*, no. 1, 2007Pearson Education Limited, 2007.

[55] P. J. Roache and P. M. Knupp, "Completed Richardson extrapolation," *Communications in Numerical Methods in Engineering*, vol. 9, no. 5, pp. 365–374, 1993.

[56] Y. A. Cengel, *Heat Transference a Practical Approach*, vol. 4, no. 9, 2004MacGraw-Hill, 2004.

[57] R. R. Bhave, *Cross-Flow Filtration*, Elsevier Inc., 3rd edition, 2014.

[58] R. Prichard, M. Gibson, C. Joseph, and W. Strasser, "A review of fluid flow in and around the brain, modeling, and abnormalities," *Multiscale Biomechanical Modeling of the Brain*, vol. 1, pp. 209–238, 2022.

[59] S. A. Marzouk, M. M. Abou Al-Sood, E. M. S. El-Said, M. M. Younes, and M. K. El-Fakharany, *A Comprehensive Review of Methods of Heat Transfer Enhancement in Shell and Tube Heat Exchangers*, vol. 148, no. 15, 2023Springer International Publishing, 2023.

[60] A. Bejan, *Advanced Engineering Thermodynamics*, 2016.

[61] E. B. Ratts and A. G. Raut, "Entropy generation minimization of fully developed internal flow with constant heat flux," *Journal of Heat Transfer*, vol. 126, no. 4, pp. 656–659, 2004.

[62] M. Awais, A. A. Bhuiyan, S. Salehin, M. M. Ehsan, B. Khan, and M. H. Rahman, "Synthesis, heat transport mechanisms and thermophysical properties of nanofluids: a critical overview," *International Journal of Thermofluids*, vol. 10, article 100086, 2021.

[63] D. Ting, "Thermofluids: from nature to engineering," in *Forced Convection*, Academic Press, 2022.

[64] S. Wu, K. Zhang, G. Song, J. Zhu, B. Yao, and F. Li, "Study on the performance of a miniscale channel heat sink with Y-shaped unit channels based on entransy analysis," *Applied Thermal Engineering*, vol. 209, article 118295, 2022.

[65] O. N. Mohanty, "Thermoanalytical methods in metals processing," in *Fundamentals of Metallurgy*, pp. 350–366, Woodhead Publishing, 2005.

[66] J. Du, Y. Hong, S. M. Huang, W. B. Ye, and S. Wang, "Laminar thermal and fluid flow characteristics in tubes with sinusoidal ribs," *International Journal of Heat and Mass Transfer*, vol. 120, pp. 635–651, 2018.

[67] X. Li, S. Liu, S. Tang, X. Mo, L. Wang, and D. Zhu, "Analysis of heat transfer characteristics and entransy evaluation of high viscosity fluid in a novel twisted tube," *Applied Thermal Engineering*, vol. 210, article 118388, 2022.

[68] V. Gnielinski, "Heat transfer coefficients for turbulent flow in concentric annular ducts," *Heat Transfer Engineering*, vol. 30, no. 6, pp. 431–436, 2009.